Journal of Molecular Structure 1237 (2021) 130419

Contents lists available at ScienceDirect

Journal of Molecular Structure

journal homepage: www.elsevier.com/locate/molstr

Charge assisted assembly of zwitterionic pyridone hydrates

Aleksandra D. Mašulović[a], Jelena M. Lađarević[b,*], Lidija D. Radovanović[a], Željko J. Vitnik[c], Vesna D. Vitnik[c], Jelena R. Rogan[b], Dušan Ž. Mijin[b]

[a] Innovation Centre of the Faculty of Technology and Metallurgy, University of Belgrade, Karnegijeva 4, Belgrade, Serbia
[b] Faculty of Technology and Metallurgy, University of Belgrade, Karnegijeva 4, Belgrade, Serbia
[c] Department of Chemistry, Institute of Chemistry, Technology and Metallurgy, University of Belgrade, Studentski trg 12-16, Belgrade, Serbia

ARTICLE INFO

Article history:
Received 1 March 2021
Revised 25 March 2021
Accepted 26 March 2021
Available online 7 April 2021

Keywords:
Computational chemistry
Hydrates
Pyridone
Stacking interactions
Zwitterions

ABSTRACT

Two pyridone derivatives, bearing the pyridinium moiety (**1**), or dimethylpyridinium moiety (**2**), have been synthesized and their crystal structures have been determined. The compounds crystalize in hydrated zwitterionic forms with either two (**1·2H$_2$O**) or four (**2·4H$_2$O**) water molecules. The zwitterionic networks contain different types of water clusters, generated into channels, incorporating them into the network by sandwiching. The type of channel depends on the crystal lattice and the nature of non-covalent interactions established between zwitterions as well as the number of water molecules incorporated into the architecture. **1** affords tubes filled in with water channels formed by water tetramers, contrary to **2**, which affords a layered network altering the zwitterionic layer and the layer formed by water tetramers and hexamers. A detailed study of intermolecular interactions of both crystal structures and a quantification of interaction energies has been performed using PIXEL lattice energy calculations, giving an insight to a quantitative evaluation of interactions through Coulombic, disperse, repulsion and polarization energies. The strongest pairwise, in both structures, is found to be a dipole–dipole interaction between oppositely charged heterocyclic rings. The differences in the crystal packings of these hydrates have been elucidated by the fingerplot analysis. The comparative studies between experimental and calculated (DFT) data of molecules **1·H$_2$O** and **2·4H$_2$O** for systems of different complexity are performed. Furthermore, correlations of experimental and calculated bond lengths and the simulation of compound solvation with the CPCM model are done.

© 2021 Elsevier B.V. All rights reserved.

1. Introduction

Considering that many pharmaceuticals exist in the form of crystalline hydrates, water clusters have received much attention both from the theoretical and experimental points of view. Various studies outlined the importance of understanding water originated hydrogen bond patterns and the ability of water to accompany organic crystals and interact with them, wherein a number of different motifs is observed [1–6]. One of the ways to understand the association of water and organic molecules is through an interplay of various non-covalent intermolecular interactions constructing complex structures. The ability of water to occupy positions in the crystal lattice and form hydrates is still an unpredictable phenomenon. It has been shown that the formation of multicomponent crystals relies on the cooperative nature of non-covalent interactions, traditionally including conventional hydrogen bonds (*e.g.*, N–H···O and O–H···O) as well as electrostatic forces and weak interactions, such as C–H···X (X = N, O, halogens, π), through the strength of intermolecular interaction between components [3,6–9]. State-of-the-art shows that frameworks containing a heteroatom in the moiety are shown to exhibit a competency to form water clusters *via* initiation of hydrogen bonds [1,6].

In this regard, 2-pyridones (2-hydroxypyridines), organic *N*-heterocyclic compounds, with a wide range of applications in chemistry and pharmacology, are known to form rigid dimers in a solid state, creating catamer motifs (head to head dimers connected into infinite chains) [10–13]. Substituted pyridones are shown to be structural units in molecules with a remarkable biological activity such as antibacterial [14,15], antifungal [16], anti-inflammatory [17], antiviral [18,19] and anticancer [20]. 2-Pyridones are also used as structural compounds in the preparation of Aβ-peptide aggregation inhibitors, responsible for amyloid

* Corresponding author.
E-mail address: jmirkovic@tmf.bg.ac.rs (J.M. Lađarević).

https://doi.org/10.1016/j.molstruc.2021.130419
0022-2860/© 2021 Elsevier B.V. All rights reserved.

formation in Alzheimer's disease [21], as well as key intermediates in the synthesis of pyridine, quinolone, quinolizidine and indolizine alkaloids [13]. The biological activity of these compounds can be closely related to the existence of the amide bond, similar to those connecting amino acids in protein molecules [22]. Also, 4,6-disubstituted-3-cyano-2-pyridones presenting both pyridines and nitriles found an application in obtaining pigments, commercial dyes and additives for fuels and oils [23]. Bearing in mind the 2-pyridone molecule architecture, it has been shown that the amino unit, traditionally being a hydrogen-bond acceptor, is in fact a hydrogen-bond donor, because of the conjugation of the lone pair on the amino N atom to the aromatic ring. On the other hand, the 2-pyridone exhibits one more tautomeric form, the hydroxypyridine molecule, which can be either a bond donor on the basis of the O atom, or an acceptor on the basis of O and N atoms [23,24]. Pyridones and pyridone derivatives are suggested as stable hydrogen bond dimers with versatile molecules in supramolecular chemistry whose aggregation patterns through hydrogen bonds are structured as cyclic dimers, one-dimensional chains or three-dimensional assemblies [11,25,26]. The 2-pyridone dimer is found to be governed by an antiparallel N–H$\cdots$O hydrogen bond forming a $R_2^2(8)$ ring as a motif [27]. Despite the existence of a strong N–H$\cdots$O hydrogen bond, the supramolecular architecture of substituted pyridone moieties is affected by secondary interactions, such as weaker hydrogen bonds as well as π–stacking interactions. The variety of structural motifs arises from altering substituents in the moieties [24,26]. To the best of our knowledge, little is known about substituted pyridone hydrates and their crystal structures have not been reported as zwitterionic hydrates so far.

Based on the above scientific background and considering wide applicability, a pyridine scaffold is introduced in the pyridone moieties. Pyridine, as a highly deficient aromatic moiety, is an interesting building block due to its ability to establish a variety of non-covalent interactions. Moreover, the pyridine salts are found to have remarkable biological activity [9,28] and salts in general are found to exhibit a tendency towards including water molecules into their crystal structure, resulting in co-crystals [1]. Co-crystals are widely applicable as magnetic materials [29], luminescent polymorphs [30,31] and solids of special optical properties [32], whereas water co-crystals have a tendency of different supramolecular formation prominence in pharmaceuticals [1,2]. It should be appointed that pharmaceuticals are often found in the zwitterionic form [2]. Zwitterions are proven to interlock quite well into crystal packing, forming dimers that stabilize the molecular architecture. Besides the strong hydrogen bonds between molecules the repeating structural segment is to be based on nonspecific interactions [4,6,33,34]. The introduction of water channels into the molecular network leads to a more stable structure, wherein zwitterions are found to incorporate water molecules into the architecture, leading to water channels [1,3,6].

In this context, the synthesis of two pyridone based zwitterion hydrates and the evolution of their crystal structures is presented. Compounds have been characterized by melting points, Attenuated Total Reflectance-Fourier transform infrared spectroscopy (FT-IR), ^{1}H and ^{13}C nuclear magnetic resonance (NMR) and mass spectroscopy (MS) as well as single-crystal X-Ray analysis. Herein, a comparative study in terms of theoretical calculation of the lattice energy of the crystal, using the PIXEL method, which gives an insight into a quantitative evaluation of interactions partitioned into Coulombic, disperse, repulsion and polarization contributions is presented. Both crystals have been compared in terms of synthesis, lattice energies and energies associated with molecular pairs extracted from their supramolecular architecture. Their DFT molecular geometries have been thoroughly analysed through the influence of dipole moments, intramolecular interactions, solvent and torsion angle influence.

2. Experimental section

2.1. General

All commercially available reagents, used without further purification, were purchased from either Fluka (Germany), Lach-ner (Czech Republic) or Sigma-Aldrich (Germany). Thin layer chromatography (TLC) was performed on silica UV254, Machereg-Nagel 0.2 mm precoated plates, a trichlormethane methanol mixture 99:1 was used. Products were visualized under UV light at 254 and 365 nm. Melting points were determined in capillary tubes on an automated melting point system Stuart SMP30. FT-IR spectra were recorded on a Nicolet iS10 (ATR) spectrophotometer. ^{1}H and ^{13}C NMR spectra were recorded on a Bruker Ascend 400 apparatus (400 and 100 MHz, respectively) in deuterated dimethyl sulfoxide (DMSO-d_6), using tetramethylsilane (TMS) as an internal standard. All spectroscopic measurements were carried out at room temperature (25 °C). MS was performed on Quadrupole ion trap mass spectrometer, LCQ Advantage (Thermo Fisher Scientific, USA) with Surveyor HPLC system (Thermo Fisher Scientific, USA).

2.2. Synthesis and crystal growth

All investigated compounds were synthesized according to a modified two step procedure [35]. Step one implies the reaction of commercially obtained 2-chloracetamide, diluted in *N,N*-dimethylformamide (DMF), and corresponding pyridine, wherein amides were acquired (Scheme 1). The second step is comprised of amides reacting with ethyl acetoacetate in methanol, under reflux, wherein pyridones **1** and **2** were obtained and recrystallized from ethanol.

Hydrates suitable for X-ray diffraction analysis were obtained from ethanol by slow evaporation during two weeks at room temperature. The molecular structures and purities of **1·2H$_2$O** and **2·4H$_2$O** were confirmed using melting points, FT-IR, ^{1}H and ^{13}C NMR spectroscopy and MS. Atoms in the compounds **1·2H$_2$O and 2·4H$_2$O** are labeled as depicted in Fig. 1 for the purpose of easier manipulation with obtained results.

2.2.1. Synthesis of 4′-methyl-2′-oxo-1′,2′-dihydro-[1,3′-bipyridin]-1-ium-6′-olate dihydrate– ***1·2H$_2$O***

Primarily, the synthesis of corresponding amide was carried out according to literature procedure [35] shown in the Scheme 1 the pathway (a). 1-(2-Amino-2-oxoethyl)-pyridinium-chloride (0.42 mol, 25 g) is diluted in 54 mL of DMF. Pyridine (0.28 mol, 21.15 g) is added to the solution and mixture was heated to 110 °C for one hour. After cooling, the obtained crude product is slurred in acetone. Further filtration and recrystallization from ethanol gives 15 g of white crystalline 1-(2-amino-2-oxoethyl)-pyridinium chloride. The obtained amide (0.1 mol, 15 g) was then diluted in 114.1 mL of methanol and then 11.14 mL ethyl acetoacetate is added along with sodium hydroxide solution (35.8 g sodium hydroxide, 90.5 mL water). The reaction mixture is stirred under reflux for three hours. The synthesis course was monitored by TLC analysis. The crude product was recrystallized from ethanol (yield 78%). The compound was further dissolved in ethanol and slow evaporation was allowed, whereas **1·2H$_2$O** is acquired. Golden crystals: m.p. > 300 °C; ^{1}H NMR (400 MHz, DMSO-d_6): δ=9.81 (s, 1H; N–H), 8.87 (d, J = 8 Hz, 2H; pyridinium), 8.52 (t, J = 6 Hz, 1H; pyridinium), 8.08 (t, J = 6 Hz, 2H; pyridinium), 4.90 (s, 1H; C4), 1.78 ppm (s, 3H; CH_3); ^{13}C NMR (100 MHz, DMSO-d_6): δ=164.10 (C5), 159.16 (C1), 148.6 (C6, C10), 145.3 (C3), 144.3 (C8), 127.7 (C7, C9), 112.34 (C2), 96.56 (C4), 17.98 ppm (CH_3); FT-IR (ATR): ν ~=1582 (vs), 1623 (vs) (C=O), 3353 (m) (N–H), 3339 (m) cm^{-1} (O–H); MS (ESI): *m/z* calcd. for $C_{11}H_{10}N_2O_2$+H$^+$:

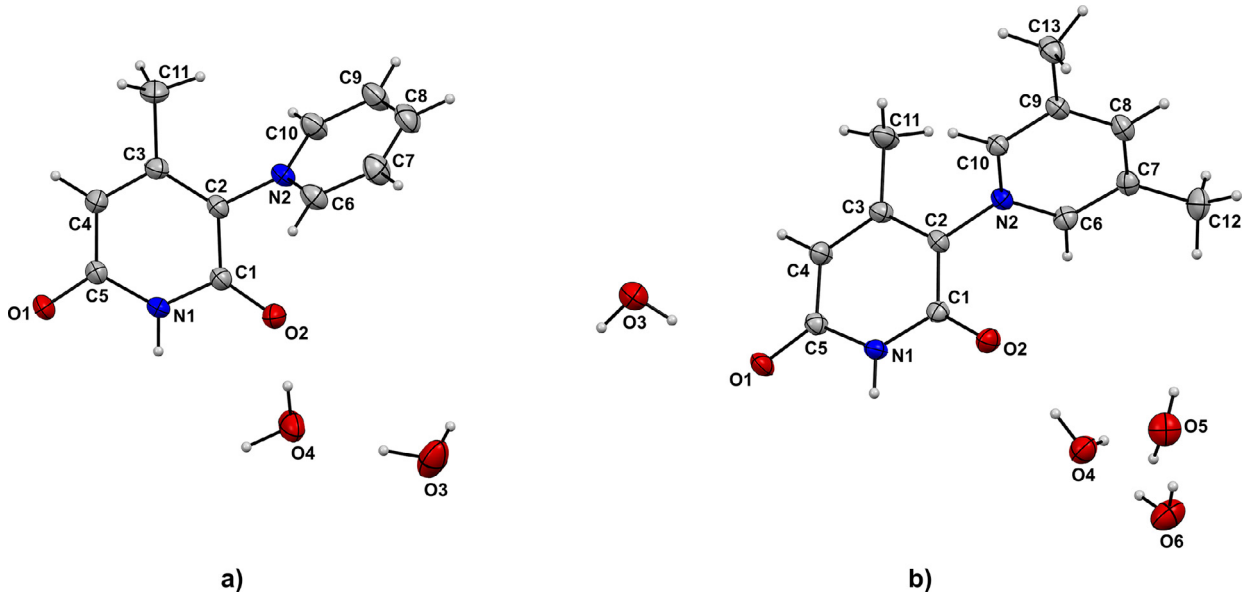

Fig. 1. The asymmetric unit of $\mathbf{1\cdot 2H_2O}$ and $\mathbf{2\cdot 4H_2O}$, with aromatic numbering scheme, showing 30% displacement ellipsoids (H atoms are presented as small spheres of arbitrary radii).

203.08 $[M+H]^+$; found: 203.27; calcd. for $C_{22}H_{20}N_4O_4+Na^+$: 427.14 $[2M+Na]^+$; found: 426.99; calcd. for $C_{33}H_{30}N_6O_6+Na^+$: 629.21 $[3M+Na]^+$; found 628.92.

2.2.2. Synthesis of 2,4,4′-trimethyl-2′-oxo-1′,2′-dihydro-[1,3′-bipyridin]-1-ium-6′-olate tetrahydrate– $\mathbf{2\cdot 4H_2O}$

The synthesis procedure for the compound **2** depicted by Scheme 1 the pathway (b) corresponds to the one for the compound **1**. The difference is in 3,5-dimethylpyridine, whereas 1-(2-amino-2-oxoethyl)-3,5-dimethylpyridin-1-ium chloride was obtained. The second step of the reaction was elongated due to an incomplete reaction according to TLC analysis and carried out for 8 h. The crude product was recrystallized from ethanol (yield 62%). The compound was further dissolved in ethanol and slow evaporation was allowed, whereas $\mathbf{2\cdot 4H_2O}$ is acquired. Orange crystals: m.p. > 300 °C; ^{1}H NMR (400 MHz, DMSO-d_6): δ =9.71 (s, 1H; N–H), 8.60 (s, 2H; pyridinium), 8.23 (s, 1H; pyridinium), 4.86 (s, 1H; C4), 2.45 (s, 6H; CH_3 pyridinium), 1.74 ppm (s, 3H; CH_3 pyridone); ^{13}C NMR (100 MHz, DMSO-d_6): δ =164.1 (C5), 159.1 (C1), 148.6 (C6, C10), 145.3 (C3), 144.3 (C8), 127.7 (C7, C9), 112.5 (C2), 96.5 (C4), 31.2 (CH_3; pyridinium), 17.98 ppm (CH_3; pyridone); FT-IR (ATR): ν ˜=1583 (vs), 1602 (vs) (C=O), 3297 (m) cm^{-1} (O–H); MS (ESI): *m/z* calcd. for $C_{13}H_{14}N_2O_2+H^+$: 231.11 $[M+H]^+$; found: 231.29; calcd. for $C_{13}H_{14}N_2O_2+Na^+$: 253.10 $[M+Na]^+$; found: 253.20; calcd. for $C_{26}H_{28}N_4O_4+Na^+$: 483.20 $[2M+Na]^+$; found: 483.05 $[2M+Na]^+$.

2.3. X-ray structure determination

Single-crystal X-ray diffraction data of $\mathbf{1\cdot 2H_2O}$ and $\mathbf{2\cdot 4H_2O}$ were collected at room temperature on an Oxford Gemini S diffractometer equipped with a CCD detector using monochromatized Mo*Kα* radiation (λ = 0.71073Å). Intensities were corrected for absorption by means of the multi-scan method. Due to the large dimensions of the single crystals of $\mathbf{1\cdot 2H_2O}$ and $\mathbf{2\cdot 4H_2O}$ (Table 1), additional Gaussian (for $\mathbf{1\cdot 2H_2O}$) and analytical (for $\mathbf{2\cdot 4H_2O}$) corrections for absorption were applied. The structures were solved by direct methods (SHELXT-2018/2) [36] and refined on F^2 by full-matrix least-squares using the programs SHELXL-2018/3 [37] and WINGX [38]. All non-hydrogen atoms were refined anisotropically. Positions of the H atoms connected to the C and N atoms were calculated on geometric criteria and refined using the riding model with U_{iso}= 1.2U_{eq}(C, N) and U_{iso}= 1.5U_{eq}(C) for the methyl group. The positions of the water H atoms were found in Δ*F* maps and added to the structural model before the final cycle of refinement with fixed coordinates and with U_{iso}= 1.5U_{eq}(O). Selected crystal data and refinement results for $\mathbf{1\cdot 2H_2O}$ and $\mathbf{2\cdot 4H_2O}$ are listed in Table 1. Crystallographic data reported in this paper have been deposited with the Cambridge Crystallographic Data centre as supplementary publication reference numbers 2057269 and 2057270 for $\mathbf{1\cdot 2H_2O}$ and $\mathbf{2\cdot 4H_2O}$, respectively. Copy of the data can be obtained, free of charge, via https://www.ccdc.cam.ac.uk/structures/.

2.4. Computational studies

All the density function theory (DFT) calculations were performed using the Gaussian 09 program package [39] with the Becke's threeparameter hybrid exchange functional [40] combined with the Lee-Yang-Parr correlation [41] functional (B3LYP) and the 6–311++G(d,p) basis set. Also, the B3LYP functional with the D3 version of Grimme's dispersion [42] was employed for comparison. The default convergence criteria without any constraint on the geometry are applied for the optimization of all investigated systems. The validity of the optimized geometries was confirmed by frequency calculations. The effect of the polar environment was approximated using the conductor polarizable continuum model (CPCM) [43,44] for the simulation of solvents with different polarities (n-hexane, chloroform, 1-butanol, n-octanol, ethanol, DMSO and water). In order to provide accurate atomic charges, natural bond orbital (NBO) calculations were performed using the NBO 3.1 program [45] at previously optimized geometries at the B3LYP/6-311++G(d,p) level in vacuum and water. A detailed crystal packing analysis on compounds $\mathbf{1\cdot 2H_2O}$ and $\mathbf{2\cdot 4H_2O}$ was performed by the PIXELC module [46,47] from CLP computer program package (version 12.5.2014). The lattice energies of the compounds were calculated and the total energy is partitioned into their Coulombic, polarization, dispersion and repulsion contributions. Molecular structures for PIXEL analysis are extracted from the X-ray structures, with hydrogen atoms relocated to their neutron values (C–H distance 1.08 Å, O–H and N–H distance 1.00 Å). The molecular electron densities for the PIXEL energy calculations were calculated at the MP2/6–31G(d,p) level. Further Hirshfeld surfaces anal-

Table 1
Crystal data and structure refinements for **1 · 2H$_2$O** and **2 · 4H$_2$O**.

Compound	1 · 2H$_2$O	2 · 4H$_2$O
Formula	$C_{11}H_{14}N_2O_4$	$C_{13}H_{22}N_2O_6$
Formula weight, g mol^{-1}	238.24	302.32
Crystal size, mm^3	0.86 × 0.38 × 0.16	0.71 × 0.28 × 0.19
Crystal system	Triclinic	Triclinic
Space group	$P\bar{1}$	$P\bar{1}$
a, Å	7.2258(14)	7.4411(15)
b, Å	8.0470(16)	10.581(2)
c, Å	11.287(2)	11.235(2)
α, °	70.71(3)	108.96(3)
β, °	74.88(3)	96.14(3)
γ, °	79.85(3)	107.41(3)
V, Å^3	595.1(2)	777.6(3)
Z	2	2
F(000)	252	324
μ, mm^{-1}	0.102	0.102
ρ_c, g cm^{-3}	1.33	1.291
θ range, °	1.959–25.341	2.945–25.341
Index ranges, h, k, l	−8→8−8→9−13→13	−8→8−12→12−13→13
Reflections collected/unique	4099/2183	5304/2847
Data/restraints/parameters	1649/4/166	2225/8/214
R indices [$I > 2\sigma(I)$]	$R = 0.0492$, $R_w = 0.1309$[a]	$R = 0.0443$, $R_w = 0.1058$[b]
R indices (all data)	$R = 0.0667$, $R_w = 0.1446$	$R = 0.0617$, $R_w = 0.1196$
Goodness-of-fit	1.033	1.042
R_{int}	0.0183	0.019
$\Delta\rho_{max}$, $\Delta\rho_{min}$, e Å^{-3}	0.311, −0.238	0.173, −0.228

[a] $w = 1 / [\sigma^2(F_o^2) + (0.0709 \cdot P)^2 + 0.2134 \cdot P]$ where $P = (F_o^2 + 2 \cdot F_c^2) / 3$
[b] $w = 1 / [\sigma^2(F_o^2) + (0.0554 \cdot P)^2 + 0.1561 \cdot P]$ where $P = (F_o^2 + 2 \cdot F_c^2) /3$

ysis [48] and the associated 2D-fingerprint plots [49] were generated using CrystalExplorer 3.1 [50].

3. Results and discussion

3.1. Synthesis

Pyridones are synthesized according to a literature procedure [35], *via* the Guareschi-Thrope condensation with corresponding 1-(2-amino-2-oxoethyl)-pyridinium-chlorides and ethylacetoacetate (Scheme 1). The yield in the case of **1** is 78%, whereas in case of **2** is 62%, which can be ascribed to the steric hindrance of the methyl groups present in the pyridinium scaffold of **2**. The synthesis of the compound **1** has been reported [35], wherein it was reported as a microcrystalline solid and was not structurally characterized, whereas compound **2** is not registered to our knowledge so far. By going through thorough analysis, it is concluded that compounds are to be found in a zwitterionic (inner salt) form in a solid state whereas resonance forms suggested for both compounds can be seen in Scheme 2. This assumption is affirmed by a MS analysis, where one proton less was found, contrary to the expected protonated form, resulting in the exact mass of 203.08 for **1** and 231.11 for **2**. The FT-IR spectra of the crystals clearly show the existence of broad O–H bands associated with water molecules centered at 3339 and 3297 cm^{-1} for **1 · 2H$_2$O** and **2 · 4H$_2$O**, respectively. Another confirmation of the hydrated forms of **1** and **2** can be seen from the 1719 and 1706 cm^{-1} bands, respectively, and can be ascribed to O–H vibrations of water molecules. The C=O vibrations are found at 1623 and 1582 cm^{-1} for **1 · 2H$_2$O** and 1602 and 1583 cm^{-1} for **2 · 4H$_2$O**. The N–H vibration of the pyridone scaffold was observed at 3253 cm^{-1} for **1 · 2H$_2$O**, whereas for the **2 · 4H$_2$O** this vibration is overlapped by the O–H band. The aromatic C–H stretching vibrations are observed in the region of 3140–3063 cm^{-1} for both compounds, while the aliphatic C–H stretching vibrations are found at 2914 and 2924 cm^{-1} for compounds **1 · 2H$_2$O** and **2 · 4H$_2$O**, respectively. The NMR spectra was according to literature analogues [51].

3.2. Geometry of pyridone molecules

Table 1 summarizes the single crystal X-ray data of **1 · 2H$_2$O** and **2 · 4H$_2$O**, while Fig. 1 depicts their molecular structures. The zwitterions contain the substituted pyridone ring (C1/C2/C3/C4/C5/N1) and the pyridinium ring (C6/C7/C8/C9/C10/N2). The compounds **1 · 2H$_2$O** and **2 · 4H$_2$O** crystallize in the triclinic space group *P*–1 with a different number of lattice water molecules in the asymmetric unit (Fig. 1). The highest distortion from planarity for the zwitterion in **1 · 2H$_2$O** is found for the C3 atom in the pyridone ring being 0.0053(3) Å and for the C10 atom in the pyridinium ring being 0.0132(5) Å. Selected bond lengths and angles, found to be in accordance with the values found for 3-cyano-6-hydroxy-4-methyl-2-pyridone [23], are presented in Table 2. The C5–O1 and C1–O2 bonds are slightly longer (1.267(3) and 1.254(3) Å, respectively) than the usual C=O bond length (about 1.20 Å) (Table 2).

The pyridone and pyridinium rings of the zwitterion in **2 · 4H$_2$O** have the biggest deviation for C5 (pyridone ring) and C7 (pyridinium ring) of 0.0149(9) and 0.0053(1) Å, respectively. The dihedral angle between two rings is slightly bigger in **2 · 4H$_2$O** than the corresponding angle in **1 · 2H$_2$O** (63.05°) and equals 68.54°. This can be ascribed to enhanced steric hindrance on the behalf of introduction of two methyl groups in the pyridinium scaffold of **2 · 4H$_2$O**. The bond lengths and angles (Table 2) are as expected for similar systems [17]. In both crystal structures, C1–O2 bond lengths are similar to C5–O1 bond lengths (Table 2). It should be appointed that the C1–O2 bond in **2 · 4H$_2$O** is slightly longer than C1–O2 bond in **1 · 2H$_2$O**, whereas C5–O1 bond lengths are almost identical for both compounds. These bond lengths were compared to the calculated ones and further discussed in details. As seen from geometry parameters of **1 · 2H$_2$O** and **2 · 4H$_2$O** in Table 2, the pyridone moieties are afflicted by the π-conjunction, sequential to two assembled heterocyclic scaffolds. The introduction of two methyl groups in the pyridinium ring of **2 · 4H$_2$O** does not have a significant impact on the change of bond lengths and angles.

Furthermore, computational methods were implied to compare data with the obtained experimental data. In light of the resolved geometry of the obtained compounds, the determined crys-

Table 2
Selected bond lengths and angles for **1 · 2H$_2$O** and **2 · 4H$_2$O**.

Bond length, Å		Angle, °	
1 · 2H$_2$O			
C5–N1	1.371(2)		
C5–O1	1.267(2)		
C1–N1	1.374(3)		
C1–O2	1.254(2)	C1–N1–C5	126.20(8)
C2–N2	1.447(3)	C1–C2–N2	115.75(7)
C3–C11	1.509(3)	C6–N2–C10	120.17(8)
C6–N2	1.342(3)	O2–C1–N1	120.27(8)
C10–N2	1.346(3)	N1–C5–O1	117.68(8)
C1–C2	1.409(3)		
C4–C5	1.399(3)		
2 · 4H$_2$O			
C5–N1	1.376(3)		
C5–O1	1.266(3)		
C1–N1	1.376(3)		
C1–O2	1.264(3)		
C2–N2	1.457(3)	C1–N1–C5	125.86(3)
C3–C11	1.505(3)	C1–C2–N2	115.67(3)
C6–N2	1.346(3)	C6–N2–C10	121.16(3)
C10–N2	1.344(3)	O2–C1–N1	119.91(6)
C7–C12	1.504(3)	N1–C5–O1	118.49(6)
C9–C13	1.498(3)		
C1–C2	1.404(3)		
C4–C5	1.404(3)		

tal structures of **1 · 2H$_2$O** and **2 · 4H$_2$O** were compared to crystal structure of 3-cyano-6-hydroxy-4-methyl-2-pyridone [23]. It is noticed that the cyano derivative crystallizes in a protonated form bearing the hydroxy group in position 6, while the compounds **1** and **2** crystallize as deprotonated forms (zwitterions). Bearing this in mind, both variants of compounds **1** and **2**, protonated-cationic (**a**) and the deprotonated zwitterion (**b**) were computationally simulated and it is substantiated that both variants are energetically possible as depicted in Figures S1 and S2 and Tables S1 and S2 (see Supplementary material). To confirm the lack of the H atom of the hydroxy group in position 6 of the pyridone moiety, NBO charges were calculated, showing that the O–H bond in the protonated form **a** of compound **1** is highly polarized (O = –0.630 e and H = 0.500 e) making this bond acidic. The calculated NBO charges for both forms of compound **1** in vacuum and water are presented in Figure S3 and Table S3. As the synthesis takes place in alkaline conditions, this leads to the formation of products in the deprotonated form **b**. Also, the simulation of deprotonation showed that the proton separation is performed without activation energy in the presence of the OH^- ion. As it can be noticed from Table S3, whether in water or vacuum, the pyridone and pyridinium scaffolds have a distinctive charge difference. NBO charge analysis shows that the structure **1b** (Figure S3b, Table S3) is overall a neutral molecule proving the assumption of the zwitterionic form of the structure. This is the consequence of the pyridone scaffold bearing a negative charge, whereas the pyridinium scaffold bears a positive one of the same absolute value.

Additionally, the comparison between the bond lengths of the determined crystal structures and DFT calculated structures of **1a**, **1b**, **2a** and **2b** indicates that the zwitterionic structures (**b**) are in fact, in much better correlation, R^2 = 0.8923 and 0.9195, than the cationic (**a**) structures, R^2 = 0.8245 and 0.8504, for compounds **1** and **2**, respectively. The experimental and computed bond lengths with corresponding correlation R^2 values are presented in Tables S1 and S2. Therefore, it can be concluded that the experimental X-ray crystal structure data and the DFT calculations confirm the zwitterionic structure for compounds **1** and **2**.

On the other hand, the correlation values R^2 = 0.8923 and 0.9195 indicate a relatively big difference between experimental and calculated structures. Usually this phenomenon is explained with fact that the DFT calculation is done for an isolated molecule. The deviations can be attributed to the non-covalent intermolecular interactions in the crystalline state which are not included in the calculation. Furthermore, calculations have been performed after the molecular network was taken into account in Section 3.5.

Moreover, the observed bond lengths for C5–O1 (1.267(3) Å for **1 · 2H$_2$O** and 1.266(3) Å for **2 · 4H$_2$O**) and C1–O2 (1.254(3) Å for **1 · 2H$_2$O** and, 1.264(3) Å for **2 · 4H$_2$O**) are longer than the usual C=O bond length (about 1.20Å [52]) due to the hydrogen bond interactions of O1 and O2 atoms (Table 3). The difference between the C1=O2 and C5=O1 bond lengths is insignificant, which can be ascribed to the extensive delocalization of the π electrons seen from the charges depicted by the NBO analysis (Figure S3). The elongation of the C=O bond, when the O atom is involved in hydrogen bonding, has been previously observed by some authors [23,53]. C5–O1 bond for both compounds is slightly longer than C1–O2 bond, because the O1 atom acts as a double acceptor in the formation of two hydrogen bonds (N1–H1A · · ·O1 and O3–H13 · · ·O1, Table 3). Another verification of the extensive delocalization of the π electrons, the O2–C1–N1 and N1–C5–O1 angles are 119.9° and 118.4° (for **1 · 2H$_2$O**) and 119.9° and 118.5° (for **2 · 4H$_2$O**), respectively. This is an indication that there is no considerable repulsion between N1 and lone pairs of O1 and O2, indicating that N1 is indeed involved in π-resonance with the carbonyl groups as stated by Gerhardt and Bolte [23]. In addition, the C1–O2 bond in **2 · 4H$_2$O** is longer than the C1–O2 bond in **1 · 2H$_2$O**, because the O2 atom in **2 · 4H$_2$O** acts as a double hydrogen bond acceptor (Table 3). The bond lengths of the pyridone scaffold fall in the range of 1.371–1.407 Å and have a π character [53]. Among these, the C1–C2 bond length (1.407 Å) for **1 · 2H$_2$O** and C1–C2 as well as C4–C5 for **2 · 4H$_2$O** (both 1.404 Å) are the longest in the pyridone moiety, which indicates a higher σ character of the bond. The reason may lay in the fact that this bond is adjacent to the pyridinium scaffold, experiencing an electron withdrawing effect [23]. It can be stated that in **2 · 4H$_2$O** the C1–C2 and C4–C5 bond lengths are identical opposite to the different electronic effects of the surrounding of these bonds. The elongation of the C4–C5 bond can be ascribed to the participation in weak bonds C4–H4 · · ·O5 interaction and O3–H14 · · ·O1 hydrogen bond (Table 3). On the other hand, pyridine scaffold bond lengths are in the range of 1.342–1.369 for **1 · 2H$_2$O** and 1.344–1.386 Å for **2 · 4H$_2$O**, fitting the range of pyridine architecture [53]. The C2–N2 bond in both compounds, connecting two rings, show σ character [53]. All of the above mentioned observations, whether experimental or calculated, lead to a conclusion that structures **1 · 2H$_2$O** and **2 · 4H$_2$O** are to be found in deprotonated, zwitterionic form.

3.3. Crystal packing of *1 · 2H$_2$O*

The compound **1** crystalizes in the triclinic space group *P*–1 with *Z* = 2. As previously discussed, zwitterions of **1** exhibit a propensity to bind the water molecules (W1 (H14O4H15) and W2 (H12O3H13)), further creating a molecular network. The crystal structure was analysed in terms of different contributing structural segments and intermolecular interactions. Interaction energies have been determined using the PIXEL method, wherein they have been divided into Coulombic, dispersion, repulsion and polarization contributions (Table 3). From the structural chemistry viewpoint, the architecture of **1 · 2H$_2$O** is governed mainly by dipole-dipole interactions, very strong hydrogen bonds, weak ones with directing capability [54], as well as π–π interactions, wherein water molecules play a significant role. 4′-Methyl-2′-oxo-1′,2′-dihydro-[1,3′-bipyridin]-1-ium-6′-olate (**1**), possessing positive charge in pyridinium scaffold and negative charge in the pyri-

Table 3
The geometries and energies (kJ mol^{-1}) of intermolecular interactions of **1 · 2H$_2$O** and **2 · 4H$_2$O** (*Cg*1 is the label for the centroid of the ring C1/C2/C3/C4/C5/N1; *Cg*2 is the label for the centroid of the ring C6/C7/C8/C9/C10/N2).

	D–H···*A*	*d*(*D*–H), Å	*d*(*D*···*A*), Å	*d*(H···*A*), Å	<(*DHA*), °	Symmetry code	E_{Cou}	E_{pol}	E_{disp}	E_{rep}	E_{tot}
Compound **1 · 2H$_2$O**											
Interactions stabilizing tube assembly	C10–H10···O1	0.930	3.192(3)	2.274	169						
	O$^-$···N$^+$		3.960			–*x* + 1, –*y*, –*z* + 1	–66.7	–21.6	–34.4	27.8	–94.9
	*Cg*1···*Cg*1		3.892(2)								
	C8–H8···O2	0.930	3.286(3)	2.897	136	–*x* + 1, –*y* + 1, –*z*	–35.4	–14.3	–25.9	14.3	–61.2
	*Cg*2 · · · *Cg*2		3.836(1)								
	*Cg*1 · · · y*Cg*1		4.924(2)			–*x* + 1, –*y* + 1, –*z* + 1	–35.1	–8.7	–32.0	10.5	–65.2
	C11–H11C · · · *Cg*1		3.167								
	N1–H1 · · · O1	0.860	2.863(2)	2.003	178	–*x* + 2, –*y*, –*z* + 1	–33.3	–23.8	–19.6	47.5	–29.2
	C9–H10 · · · O1	0.930	3.334(3)	2.559	141	*x*–1, *y*, *z*	–9.9	–5.8	–11.6	4.1	–23.2
Interactions between tube and water channel	O4–H14 · · · O2	0.849	2.694(3)	1.847	175	*x*, *y*, *z*	–68.6	–25.4	–18.7	58.8	–53.9
	O4–H15 · · · O1	0.847	2.738(3)	1.942	156	–*x* + 2, –*y*, –*z* + 1	–41.1	–12.2	–8.1	27.0	–34.3
	C4–H4 · · · O3	0.930	3.477(3)	2.578	163	*x*–1, *y*, *z* + 1	–1.0	–2.2	–5.4	3.6	–5.0
	C6–H6 · · · O3	0.930	3.071(4)	2.333	136	–*x* + 2, –*y* + 1, –*z*	–16.8	–5.4	–8.7	9.6	–21.7
Interactions in water channel	O3–H13 · · · O4	0.847	2.795(3)	1.952	173	*x*,*y*,*z*	–32.5	–9.0	–8.3	16.7	–33.1
	O3–H12 · · · O4	0.847	2.894(4)	2.065	166	–*x* + 2, –*y*, –*z*	–37.4	–11.6	–7.0	24.2	–31.8
Compound **2 · 4H$_2$O**											
Interactions in zwitterionic layer I	C6–H6 · · · O1[a]	0.930	3.126(3)	2.501	125						
	*Cg*1 · · · *Cg*1		3.691(1)			–*x* + 1, –*y* + 1, –*z* + 2	–54.8	–18.9	–41.2	26.5	–88.3
	N$^+$–O$^-$		3.852								
	C13–H13C · · · *Cg*1[a]		2.845			–*x* + 1, –*y* + 1, –*z* + 1	–30.2	–10.5	–35.9	20.5	–56.1
	N1–H1 · · · O1	0.860	2.863(2)	2.011	170	–*x* + 2, –*y* + 1, –*z* + 2	–29.6	–23.1	–18.7	45.4	–25.9
	C12–H12A · · · O2	0.960	3.449(3)	2.519	163	*x*–1, *y*, *z*	–9.5	–5.6	–9.8	4.4	–20.5
	C13–H13B · · · *Cg*2[a]		3.219			–*x*, –*y*, –*z* + 1	–13.9	–5.9	–16.6	5.4	–30.9
	*Cg*2 · · · *Cg*2		5.396(1)								
Interactions between layers	O3–H14 · · · O1	0.848	2.728(2)	1.884	174	*x*, *y*, *z*	–43.6	–14.5	–10.5	33.5	–35.1
	C8–H8 · · · O5	0.930	3.438(3)	2.753	131	–*x*, –*y*, –*z* + 1	–13.2	–2.4	–5.5	2.8	–18.4
	O6–H21 · · · O2	0.846	2.973(2)	2.141	168	–*x* + 1, –*y*, –*z* + 1	–37.3	–9.6	–13.0	14.1	–45.8
	C10–H10 · · · O6	0.930	3.331(3)	2.504	148						
	C11–H11C · · · O6	0.960	3.875(3)	2.949	162	*x*, *y* + 1, *z*	–15.1	–4.9	–9.5	7.2	–22.3
	C13–H13A · · · O6	0.960	3.563(3)	2.672	154						
	O4– H17 · · · O2	0.851	2.757(2)	1.914	171	*x*, *y*, *z*	–79.2	–26.0	–21.0	60.7	–65.5
Interactions in water layer II	O5–H19 · · · O3	0.840	2.813(3)	1.981	170	*x*–1, *y*–1, *z*	–39.0	–10.8	–7.2	22.1	–35.0
	O3–H15 · · · O4	0.847	2.843(3)	2.001	173	–*x* + 2, –*y* + 1, –*z* + 2	–29.9	–10.1	–9.7	21.0	–28.7
	O5–H18 · · · O3	0.814	2.876(3)	2.047	169	–*x* + 1, –*y* + 1, –*z* + 2	–24.4	–8.6	–10.5	17.1	–26.4
	O4–H16 · · · O5	0.849	2.797(3)	1.956	171	*x*, *y*, *z*	–23.7	–10.0	–8.8	24.6	–17.8
	C4–H4 · · · O5	0.930	3.603(3)	2.697	165	–*x* + 1, –*y* + 1, –*z* + 2	–37.2	–11.1	–11.4	18.9	–40.8
	O6–H20 · · · O4	0.930	3.126(3)	2.501	125	*x*, *y*, *z*	–30.0	–8.2	–5.5	11.3	–32.4

[a] Double interactions oriented in two directions, connecting dimers.

done moiety, showed the existence of strong intermolecular interaction between the pyridone and pyridinium moieties.

The pairwise involving the zwitterionic molecules, has interaction energy of –94.9 kJ mol^{-1}, along with C–H · · · O and π–π interactions (Table 3, Fig. 2, structural segment **A**). The cationic pyridinium ring acts as a charge acceptor to the negatively charged part of the pyridone moiety originating from the deprotonated O1 atom, as formerly observed from the computational analysis. This interaction bears the highest energy (Table 3), wherein Coulombic contribution, being –66.7 kJ mol^{-1}, shows that electrostatics significantly contribute to the strength of this intermolecular interaction. Due to this zwitterionic intermolecular interaction, as well as strong double C–H · · · O interactions and the face to face π–π interaction between two pyridone moieties (*Cg*1 · · · *Cg*1 distance 3.892(2) Å), the zwitterionic dimers are connected along the *c*-axis (structural segment **A** in Figs. 2 and 3a). It is worth mentioning that along with the strong hydrogen bonding capability of the O1 and N1 atoms of the pyridone scaffold, the zwitterionic molecule adopts more features. As the positive charge of the pyridinium ring attracts the neighboring pyridone moiety through a charge assisted hydrogen bond, so too does the pyridinium moieties create hydrophobic parts, also stabilized by C–H · · · O and π–π interactions (Fig. 3a). Pyridine moieties are aggregated by parallel-displaced π–π interactions (*Cg*2 · · · *Cg*2 distance 3.836(1) Å) that facilitate the formation of R_2^2 (16) ring by a pair of C–H · · · O interactions depicted by structural segment **B** (Fig. 2). The crystal packing is also stabilized by π-systems of two pyridone rings at a large offset *Cg*1 · · · *Cg*1 (distance of 4.924(2) Å), where the dispersion plays the major role (Table 3) along with the C11–H11C · · · π interaction (Fig. 2, structural segment **G**). The above-mentioned interactions ease a formation of a chain along the *c*-axis (Figs. 2 and 3a). On the other hand, inversion related dimers are connected by N–H · · · O synthon along the *a*-axis previously reported as a main factor for stability of the molecular network [23].

The N1 atom of the pyridone scaffold is the hydrogen bond donor that interacts with the carbonyl O1 atom of the adjacent molecule facilitating the formation of a centrosymmetric R_2^2 (8) ring. Moreover, N–H · · · O hydrogen bonds (Fig. 2, structural segment **C**) are conveying a significant repulsion contribution to the cumulative energy value of the interaction, on account of the O1 atom having an anionic character, which results in a greater repulsion of lone pairs, *eo ipso*, in a greater angle than expected (Table 2). As seen from Fig. 3a, contacts along the *c*-axis allow zwitterionic molecules to form an infinite chain, whereas along the *a*-axis a zigzag chain structure allows the formation of hollow spaces in a 3D space (Fig. 3b). Subsequently, the tube [55] assembly is characterized by the strong Coulombic term (Table 3). Nevertheless, the dispersion term drives the relative orientation of molecules, resulting in the formation of the tubes in crystal packing of the **1 · 2H$_2$O**. Further, hollow spaces formed by the

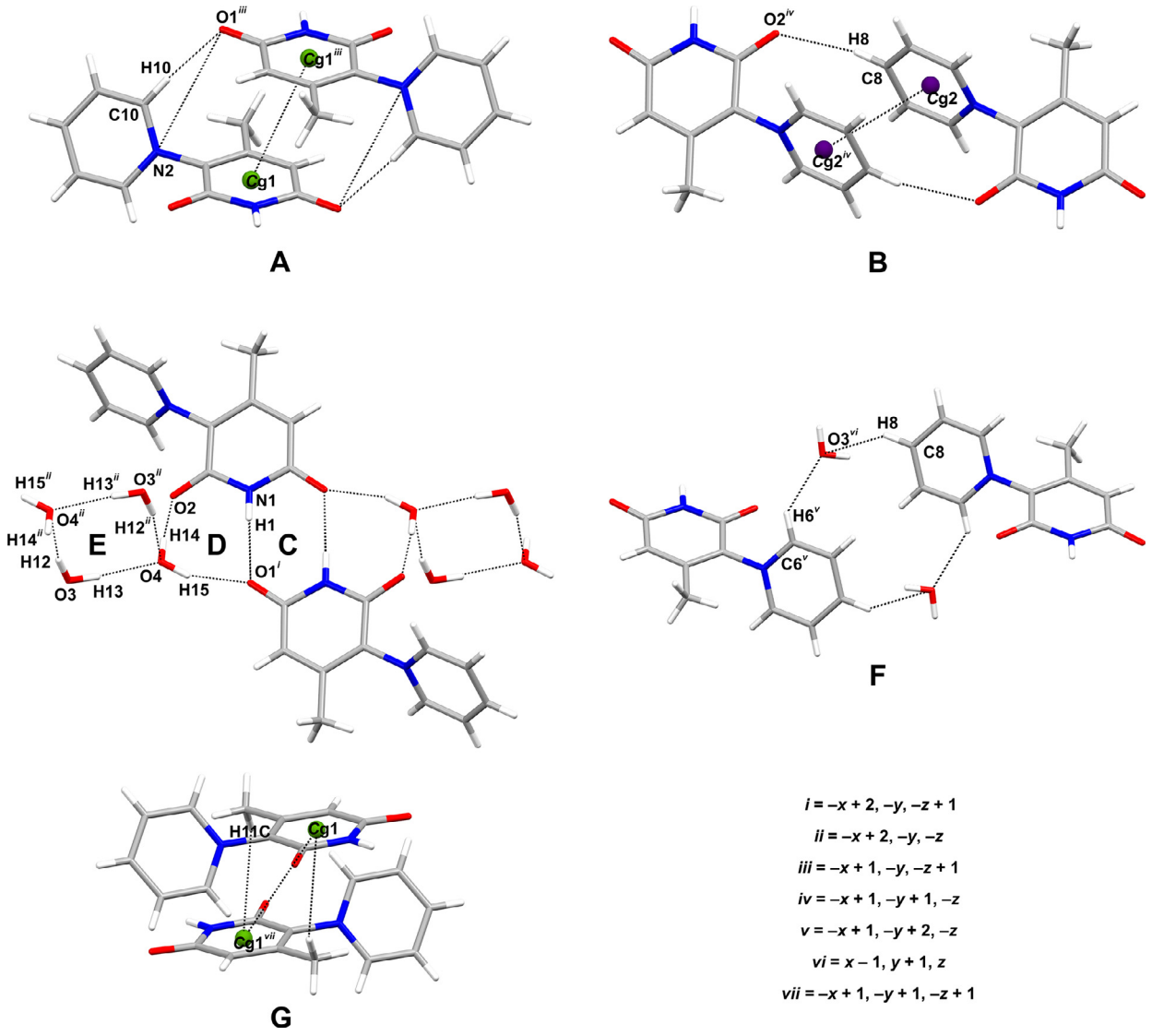

Fig. 2. Observed structural segments stabilizing the supramolecular network of $\mathbf{1 \cdot 2H_2O}$.

zwitterion tubes are filled in with water molecules, forming water channels. The tubes and channels are connected *via* hydrogen bonds. Fig. 3a shows that the hydrogen bonded water molecules form a tetrameric pseudo ring motif [6] (Fig. 2, structural segment **E**). These tetramers are sandwiched between neighboring zwitterionic molecules, thus creating the above-mentioned water channels. Therefore, the final architecture of $\mathbf{1 \cdot 2H_2O}$ is influenced both by zwitterionic π-π interactions forming tubes and water hydrogen bonded tetrameric pseudo rings. In light of resolving the contacts between water channels and zwitterionic molecules, it should be appointed that water molecules are located in a way that W1 interacts with a zwitterion creating structural segment **D**. These pairwise intermolecular interactions were estimated to be –53.9 kJ mol^{-1} and –34.9 kJ mol^{-1}, therefore significantly contributing to the total stability. Furthermore, the W1 molecule acts as a hydrogen bond acceptor to a W2 (**E**). In addition, W2 connects inversion related dimers of zwitterions by C6–H6$\cdots$O3$\cdots$C8–H8 structural segment **F** (Fig. 2). A weak C4–H4$\cdots$O3 interaction (Figure S4) connects the pyridinium part of the zwitterion with water channels, while W2 is connected through strong O4–H15$\cdots$O1 and O4–H14$\cdots$O2 hydrogen bonds. Moreover, W1 is connected to the zwitterion moiety through hydrogen bonds (Fig. 2, structural segment **F**) stabilizing the infinite chain of zwitterion molecules through one water molecule. It is worth mentioning that the number of potential donors surrounding the O1 atom from the carbonyl group, leads to bifurcated role of this atom, with the utilization of two hydrogen bonds.

3.4. Crystal packing of $\mathbf{2 \cdot 4H_2O}$

The molecular structure of the compound $\mathbf{2 \cdot 4H_2O}$ adopts triclinic space group *P*–1 with *Z* #x00A0;2. The asymmetric unit comprises of zwitterion molecule **2** and four water molecules (W1 (H14O3H15), W2 (H16O4H17), W3 (H18O5H19) and W4 (H20O6H21)). In accordance with the performed analysis (Table 3), the crystal packing of $\mathbf{2 \cdot 4H_2O}$ is depicted in Fig. 4. The hydrogen bonds characterized by the dominant Coulombic term, drive the zwitterion tetrahydrate to form layers. Two different types of layers are formed, one by the zwitterion molecules (Fig. 4. I, zwitterion layer), and the other one made by the water molecules (Fig. 4. II, water channels layer). Nevertheless, the orientation of zwitterion molecules within layer I is in addition to the Coulombic energy controlled by interactions with the strong dispersion term, causing stabilization. The layers I and II are stabilized by hydrogen bonds.

Within the zwitterion layer I, intralayer stabilization involves the zwitterionic molecules of $\mathbf{2 \cdot 4H_2O}$, which is in agreement with

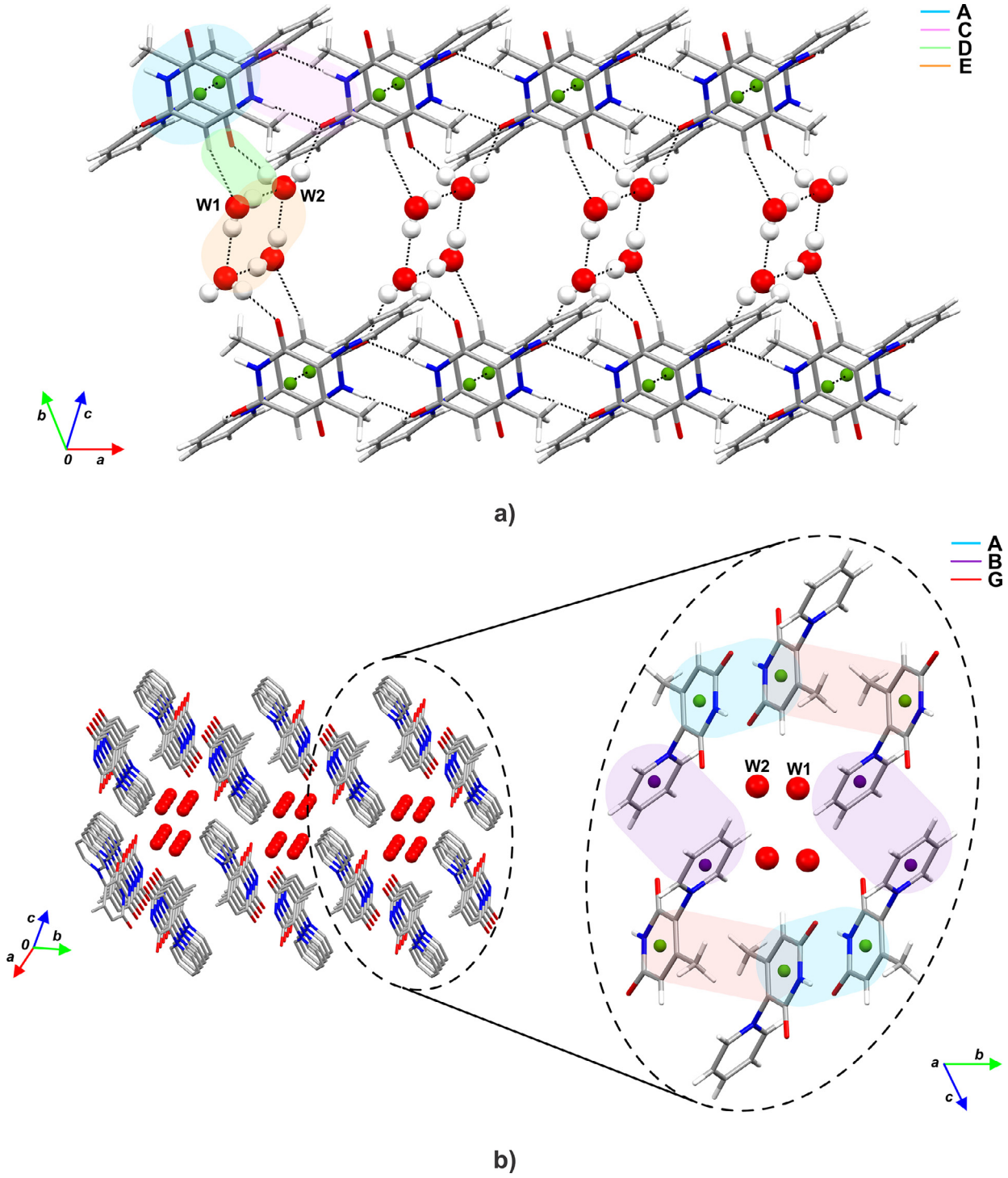

Fig. 3. The crystal packing of $\mathbf{1 \cdot 2H_2O}$ with highlighted structural segments.

the crystal packing of $\mathbf{1 \cdot 2H_2O}$. The pairwise interaction is estimated to be –88.3 kJ mol^{-1}, bearing distinctive charge separation in the scaffolds and mainly contributing with the Coulombic contribution of –54.8 kJ mol^{-1} to total energy. As in the zwitterion of $\mathbf{1 \cdot 2H_2O}$, the electronegative part of the pyridone scaffold interacts with the electropositive part of the pyridinium moiety stabilizing dimers by dipole-dipole interaction. This interaction with the assistance of hydrogen bonds and π–π interactions (*Cg*1 · · · *Cg*1 distance 3.691(1) Å) result in inversion related dimers (Fig. 5, structural segment **G**). Along the *c*-axis, a pair of C13–H13C · · · π interactions (**H**) links the adjacent zwitterionic dimers.

The C and H atoms involved, originate from the introduced methyl groups in the pyridine moiety and the π-system of the pyridone ring (Figs. 4 and 5). The altering of hydrogen bond assisted dipole-dipole, π–π and C–H · · · π interactions constructs an infinite chain of zwitterion moieties almost parallel to the *c*-axis. From the other perspective, along the *a*-axis, the pyridone molecules form dimers *via* N–H · · · O hydrogen bond, forming a $R_2^2(8)$ ring (**A**). In addition to the ring synthon, the orientation of two pyridinium scaffolds results in yet another π–π interaction (Fig. 5 structural segment **J**). Additionally, this segment, **J**, is strengthened by C13–H13B · · · π contacts. The large offset of these

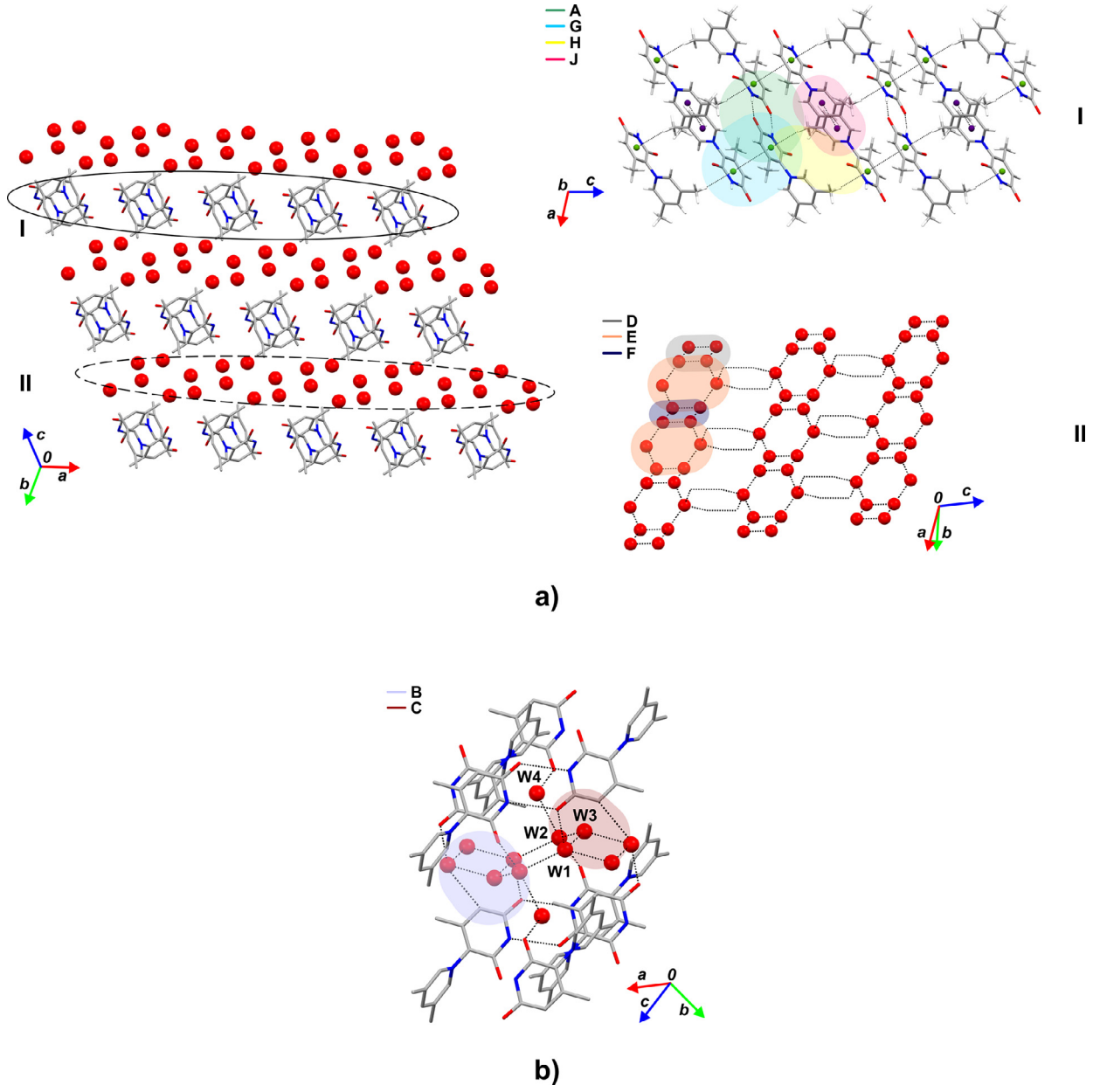

Fig. 4. The layered crystal packing of **2 · 4H$_2$O** (I–zwitterion layer, II-water channels layer) (a); interactions between layers (b).

π-stacking interactions results from the steric hindrance of the methyl groups of the pyridinium scaffold of **2 · 4H$_2$O**. The alteration of the N–H · · · O motif with the π–π interaction allows the formation of another chain of zwitterionic moieties approximately along the *a*-axis. The two chains are interlacing, creating a layer of the zwitterionic molecules (Fig. 4). As seen from Table 3 and Fig. 4, this layer consists of an interplay of two chains, which are mainly electrostatic and dispersion driven.

The association of layers I and II can be explained by the fact that, the zwitterion contains a group of proton donors and proton acceptors, wherein it shows a strong affinity towards hydrogen bonding, incorporating the water molecules. The O1 atom of the pyridone core is the H-bond acceptor to the molecule W1 that concurrently interacts with another water molecule W2 as the donor (O3–H15 · · · O4) as seen from **C**. Simultaneously, the same water molecule, W1, acts as the acceptor for the third water molecule W3 (**D**). In this manner, the zwitterion layer is connected with the water layer through hydrogen bonds displayed in Fig. 4b. The O1 atom, has trifurcated role, manifested through N1–H1 · · · O1, C6–H6 · · · O1 and O3–H14 · · · O1 interactions (Fig. 5).

Compound **2 · 4H$_2$O** shows a layered structure with π-stacked interactions within the zwitterionic layer, whereas the water layer is forged by hydrogen bonds. It is important to mention that zwitterion-water hydrogen bond also stabilizes adjacent zwitterion dimers, allowing the formation of a supramolecular 3D network, as presented in Fig. 4. The H · · · O distance varies between 1.847 and 2.897 Å, the slightest being between pyridone and the water molecule (O4–H14 · · · O2). The shorter the H · · · O distance is, the greater the Coulombic energy contribution, as well as the repulsion of the atoms. Interestingly, the C12–H12•••O2 interaction (structural segment **I**), interconnects the rings in different symmetries facilitating the formation of 3D supramolecular network, being the weaker hydrogen bond with a total energy of –20.5 kJ mol^{-1} with directing capability [54].

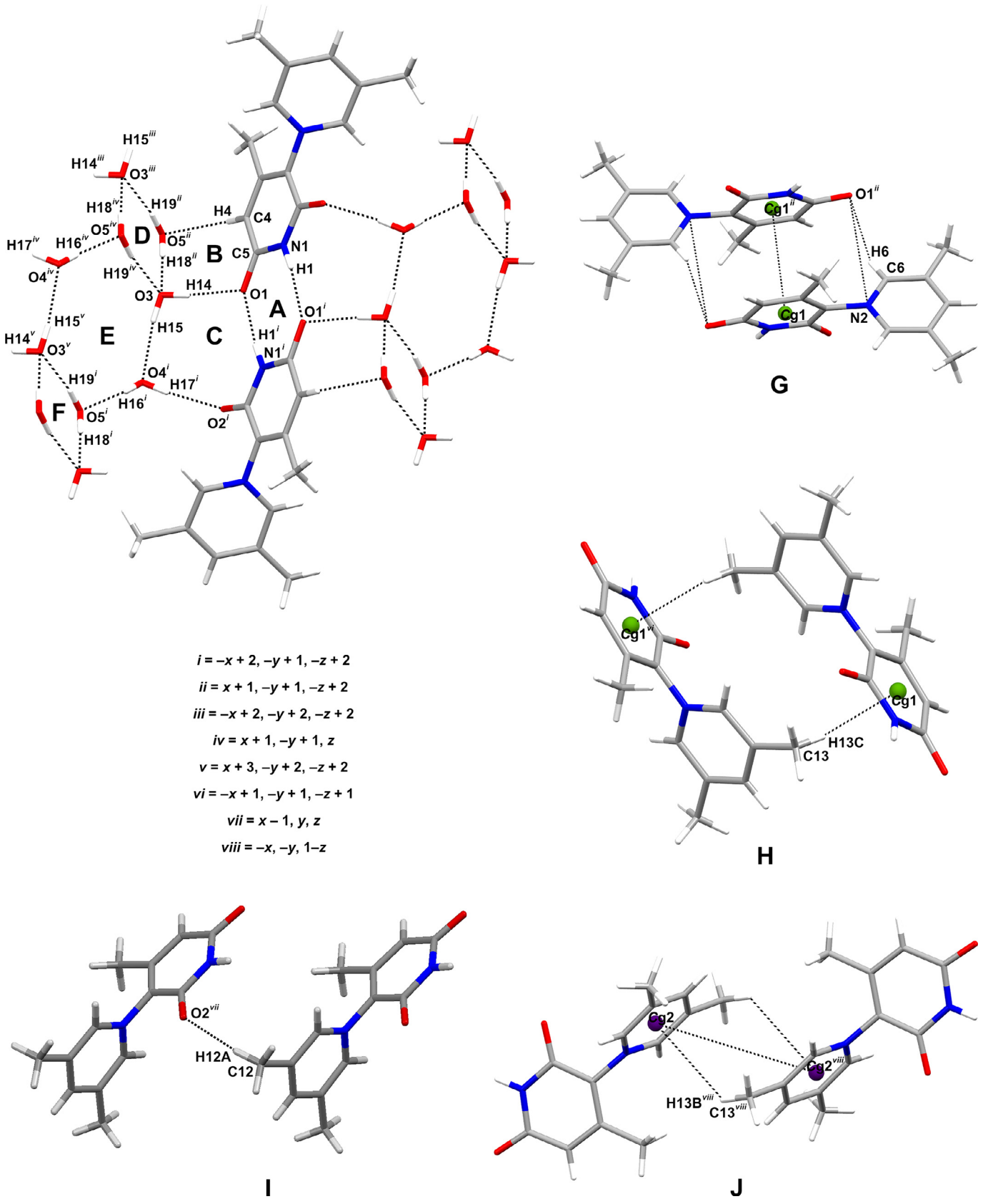

Fig. 5. Observed structural segments stabilizing supramolecular network of **2**·4H_2O.

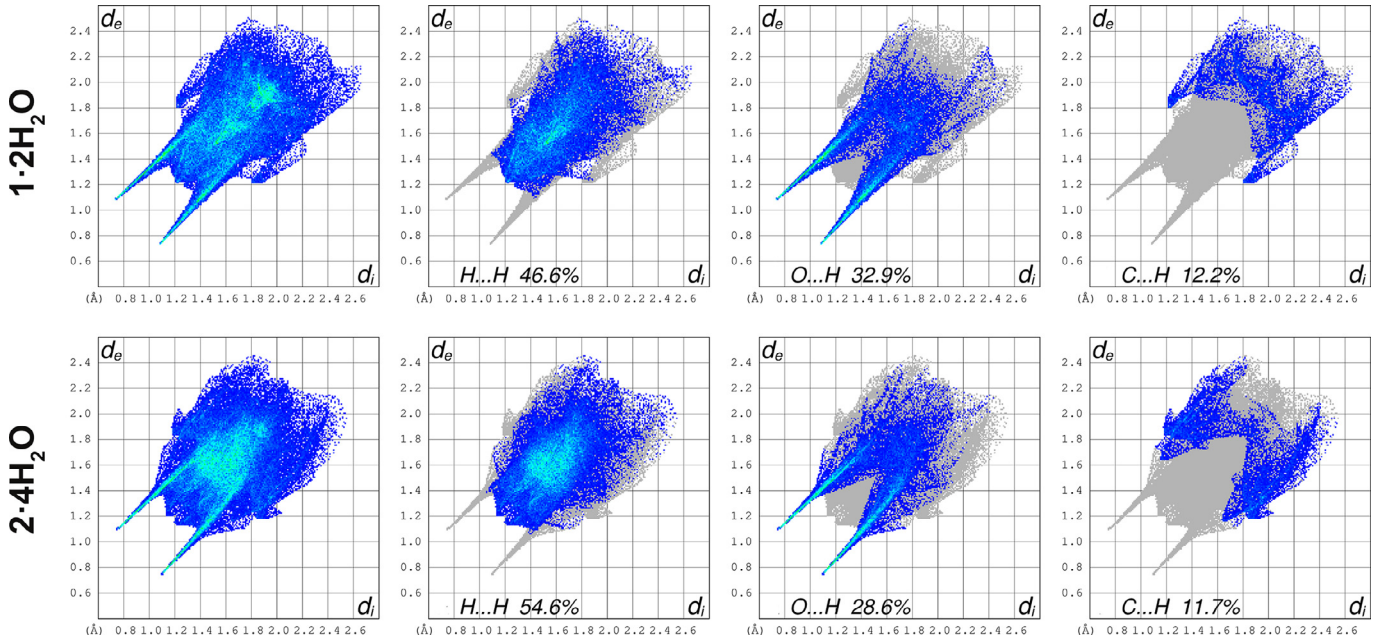

Fig. 6. 2D fingerprint plots of **1 · 2H$_2$O** and **2 · H$_2$O** showing percentages of contacts contributed to the total Hirshfeld surface area.

The water layer II is, as expected, derived and oriented by Coulombic interactions. Mainly, water molecules are interconnected in tetrameric and hexameric pseudo rings (**D**, **E**), whereas O6 is not included in these structural segments, having a role only in the interconnection of the layers (Figure S5). **D** and **E** structural segments are edge-fused and form an infinite chain along the *a*-axis. The chains are connected through zwitterion–water hydrogen bonds creating water channels in the layer (Fig. 4). Supramolecular architectures of compounds **1 · 2H$_2$O** and **2 · 4H$_2$O** are similar with noticeable differences. Both have strong Coulombic contributions derived for dipole-dipole interaction, but for **1 · 2H$_2$O** this interaction is directional, contrary to **2 · 4H$_2$O**, where a large offset of the interaction prevents Coulombic forces to direct assembly. Moreover, both zwitterionic molecules in the architectures are held together by N–H · · · O hydrogen bonds, making the same, isostructural synthon in supramolecular structures (Fig. 2 structural segment **C** for **1 · 2H2O**, Fig. 5 structural segment **A** for **2 · 4H$_2$O**). The main difference of the assembly comes from the greater number of water molecules in the packing of **2 · 4H$_2$O**. Moreover, methyl groups of compound **2 · 4H$_2$O** prevent contacts of zwitterions along the *b*-axis creating the hollow spaces of water channels and preventing the formation of zwitterion tubes as in **1 · 2H$_2$O**. This results in the appearance of the new water constructed layer, contrary to four membered pseudo rings present in the crystal packing of **1 · 2H$_2$O**, where the water channels are formed.

The 2D fingerprint plots of compounds **1 · 2H$_2$O** and **2 · 4H$_2$O** are displayed in Fig. 6, while overall interaction contributions are depicted in Fig. 7. These plots represent underlying differences between hydrates, thus highlighting the distinctions in the crystal environments due to the presence of either two or four water molecules. For both structures, we can observe two long sharp spikes, characteristic for strong hydrogen bonds (O · · · H) [54,56]. The main difference in the plots is presented in the wings associated with C · · · H weak interactions. The shape and nature of decomposed structures is similar for **1 · 2H$_2$O** and **2 · 4H$_2$O**, whereas a slightly bigger contribution of H · · · H and C · · · H interactions in the structure **2 · 4H$_2$O** can be observed. The difference is due to the presence of two methyl groups in the pyridinium scaffold as well as two additional water molecules. Contrary to the existence of two extra water originated oxygen atoms in **2 · 4H$_2$O**, the contribution of strong hydrogen bond O · · · H is larger in the case of structure **1 · 2H$_2$O** over the fingerprint surface. In both cases, H · · · H contacts were found to have the highest contributions with a similar magnitude. The interesting feature on the fingerprint plot is found in the case of π-π stacking (C · · · C) contact (Figures S6 and S7), showing that crystal packing of **1 · 2H$_2$O** is more stabilized with this interaction than the crystal packing of **2 · 4H$_2$O**. Supplementary material contains fingerprint plots of the pyridone structures **1** and **2** without interactions with adjacent water molecules. The fingerprint plots of the sole pyridone molecules indicate that most of the H · · · H and O · · · H interactions originate from the pyridone molecule itself. This can be seen from the fact that their contribution is supreme even if the water molecules are not included in the calculations. Moreover, the interesting feature is that C · · · H contributions are significant, whether water is present in the calculation or not, and greater in the crystal packing of **2 · 4H$_2$O**.

3.5. Computation simulation of molecular network

The intermolecular hydrogen bonding interactions are energetically the most important non-covalent interactions persistent in these studied compounds. Insight into the experimentally determined structures of compounds **1 · 2H$_2$O** and **2 · 4H$_2$O** shows that their complexity is primarily determined by a large number of these bonds between parent molecule and the water molecules present in the unit cell. To examine the impact of the inclusion of additional hydrogen bonds (such as dimeric counterpart and water molecules in their different arrangement) into the simulated systems for appropriate structure determination, we conducted the comparative studies between experimental and calculated (DFT) data of compounds **1 · 2H$_2$O** and **2 · 4H$_2$O** for systems of different complexity. At the same time, we tried to determine the minimal system needed to be taken into account when computing molecular geometry for such complex crystal systems.

Several systems have been defined, **c**-**f**, wherein complexity as well as the number of hydrogen bonds has been increased continuously, and are shown in Figures S1 and S2 (see Supplementary material). Defined systems are fully optimized with the B3LYP/6–311++G(d,p) method. The calculated bond lengths are compared

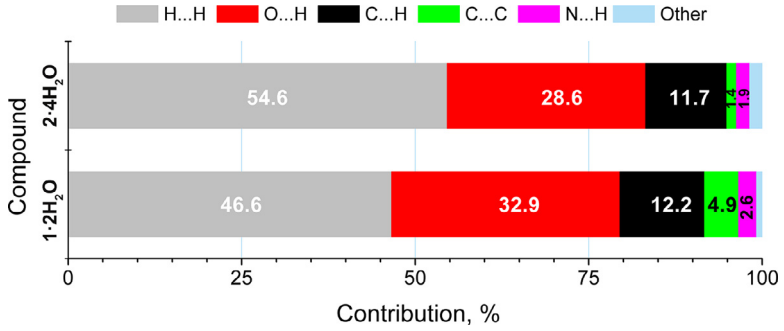

Fig. 7. Relative contribution of intermolecular atom–atom contacts to the Hirshfeld surface area.

with experimental ones and the results are presented in Tables S1 and S2 for compounds **1 · 2H$_2$O** and **2 · 4H$_2$O**, respectively. As non-covalent interactions such as intermolecular hydrogen bonds in typical CHON-based molecular solids, are always underestimated by standard DFT empirical dispersion correction the D3 version of Grimme's dispersion [42] was employed for comparison. As seen from Tables S1 and S2, the introduction of the additional molecules into the system significantly improves the correlation between the experimental and calculated bond lengths. This quality correlation increase is particularly apparent in systems **1d** and **2d** with dimeric structures which are further strengthened by hydrogen bonds over the water molecule bridges.

The introduction of two additional water molecules (systems **e** and **f**) also contributes to the increase in the quality of correlations, but the level depends on the position of the added water molecules. In the system **1e**, four water molecules arranged as in the X-ray structure of **1 · 2H$_2$O** improve the correlation to a greater extent than it is the case with system **1f**, where the water molecules are arranged as in the X-ray structure of compound **2 · 4H$_2$O**. At the same time, when comparing the quality of correlations for **2 · 4H$_2$O**, a system **2f** with four water molecules gives a better correlation than system **2e**. Furthermore, it can be concluded that the correct arrangement of water molecules is an important parameter for obtaining a good correlation.

The introduction of empirical dispersion correction (D3) in the calculation for an isolated molecule, without intermolecular interactions (systems **b**), leads to a decrease in correlation compared to the standard B3LYP calculation, while in all other systems (**c**–**e**) in which these interactions are present there is a small but continuous increase in correlation quality. The system **f** is not stable under B3LYP-D3 calculation conditions. Comparing the differences between the calculated and experimental bond lengths, it can be noticed that the largest discrepancies in the bond length, (Δ_{Max} ~ 0.045 Å) occur in the C1–C2 and C4–C5 bonds length, which indicates an insufficient delocalization of the electron density through these bonds. As the system complexity increases, these deviations decrease (~ 0.035 Å for system **e** and **f**) and standard deviation (SD), falling below 0.02 Å which can be stated as good and reliable compared to the experimental lengths. Comparing other experimental geometric parameters with the theoretically calculated ones, it can be seen that the largest deviation originates from the torsion angle between the twisted pyridone and pyridinium planes. The experimentally determined values are 63.05 and 68.54° for **1 · 2H$_2$O** and **2 · 4H$_2$O**, while the theoretically calculated values are 44.2 and 45.6°, respectively. In order to shed a light on the reasons of such an unusually large deviation between the experimental and calculated torsion angles as well as its consequential influence on the bond lengths we decided to additionally investigate this phenomenon.

The biphenyl is the simplest and thus the most commonly studied system in which planarity distortion of phenyl planes occurs. The study generates the traditional picture that an energetic competition between the favourable π-conjugation pairing the two phenyl rings and the steric repulsion within the adjacent hydrogens in *ortho*-position, are decisive parameters for the torsion angle between the two twisted phenyl planes [57]. Also, the potential energy surface (PES) of the relative torsion angle of the phenyl planes shows that the PES near the minimum is very shallow and the torsion angle can be easily changed under external influences.

The PES for the relative torsion angle between pyridone and pyridinium planes for compounds **1** and **2** was done by optimizing all coordinates except the torsion angle. The part of PES for compound **1** is shown in Fig. 8 while the whole comparable PESs for compounds **1** and **2**, as well as for the biphenyl, are shown in Figure S8.

By comparing the energies of the transition states, TS1 and TS2, it can be seen that they are significantly higher than those of biphenyls (see Figure S8). The significantly higher energy of TS1 can be attributed to the presence of a methyl group in the position 4 of the pyridone ring. On the other side, the higher energy of the TS2 state indicates a significant increase in the resonance energy due to a significant shift of electron density from the pyridone to the pyridinium scaffold.

The introduction of the additional methyl groups in the *meta*-positions of the pyridinium scaffold (compound **2**) slightly increases the steric repulsions and thus increases the energy of TS1. Simultaneously, the methyl groups with their $+I$ inductive effect stabilize the positive charge from the pyridinium ring and thus reduce the resonance between the two scaffolds, therefore the energy of the TS2 state is reduced. As a consequence, a slight increase appears in the calculated planarity distortion relative to the compound **1** of about +1.4°.

Nevertheless, it is known that a significant redistribution of electron density and polarization of the molecules may be caused by the polarizing influence of molecular surroundings in the crystal phase [58].

In the solid state the interactions between the molecules are usually governed by dipole–dipole interactions, where an increase of the molecular dipole moment leads to the stabilization of the crystal packing. Table 3 gives an insight that the energetically strongest interactions stabilizing the zwitterion in **1 · 2H$_2$O** in solid state, through a proper arrangement of **A** and **C**, belongs to dipole-dipole interactions between two parallel molecules with oppositely oriented dipoles (E_{Pol} of −21.6 and −23.8 kJ mol^{-1}). The energies of these interactions are large enough to compensate the energy consumed for increasing the torsion angle, which therefore increases the polarization within the molecule as well as its dipole moment. To see to what extent the simulation of this dipole–dipole interaction affects the torsion angle as well as the calculated bond lengths, systems **1g** and **2g** are defined and optimized.

The geometries of these systems are shown in Figure S9 and the calculated bond lengths are given in Tables S4 and S5 to-

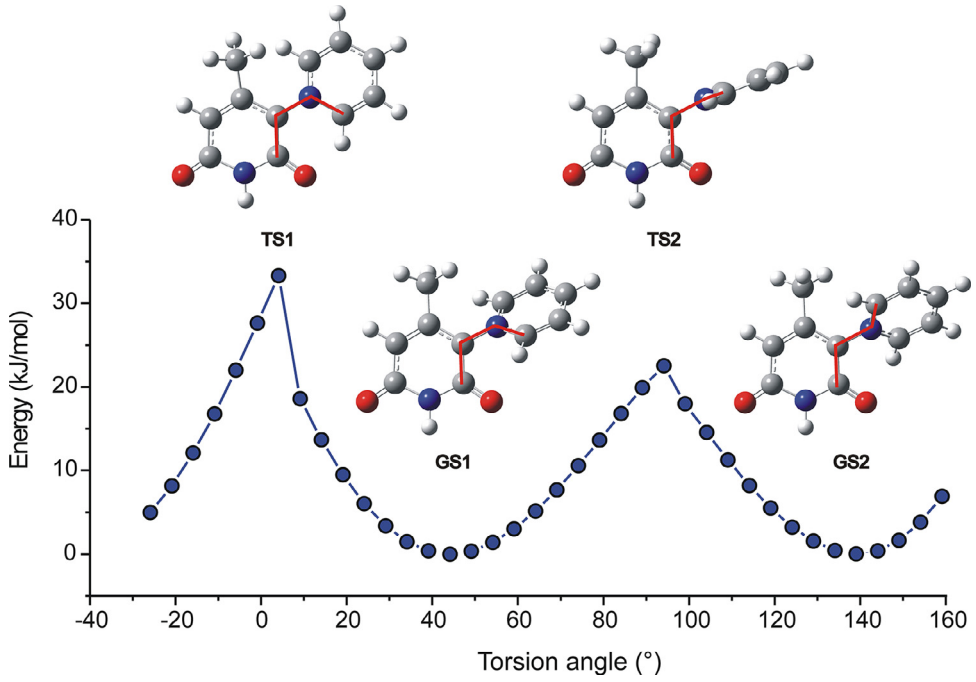

Fig. 8. The part of PES of the torsion angle for the pyridone and pyridinium planes of zwitterionic moiety in **1**.

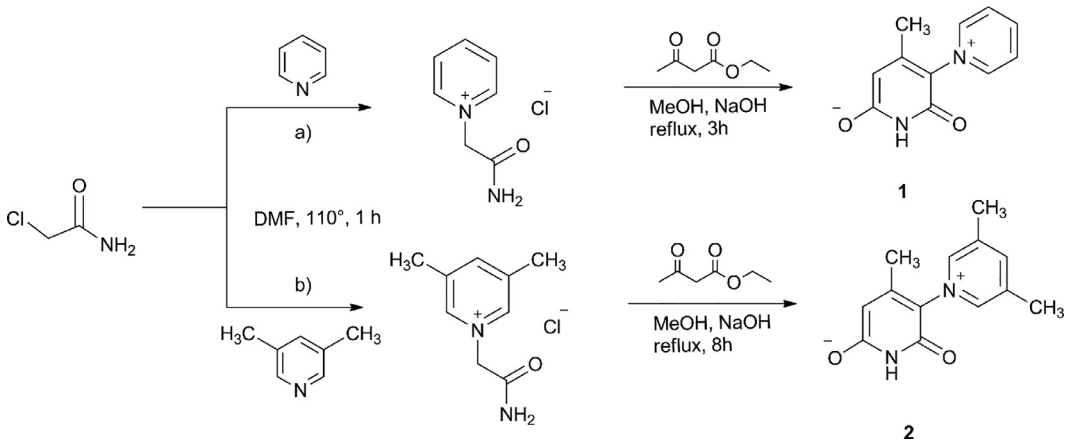

Scheme 1. Synthetic pathway of **1** (a) and **2** (b).

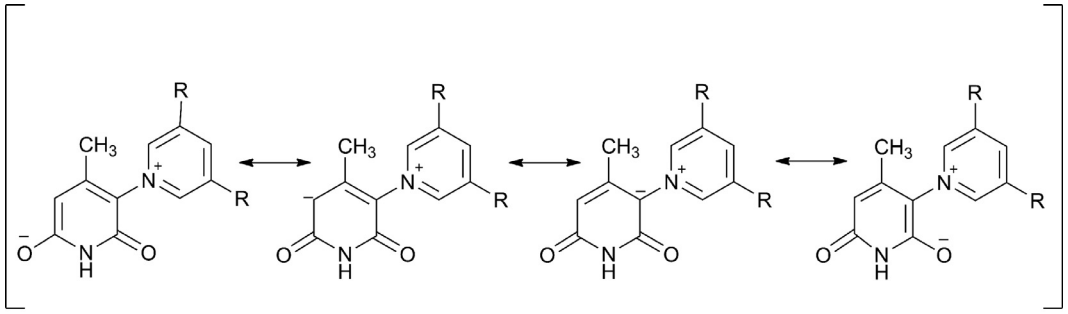

Compound	R
1	-H
2	-CH_3

Scheme 2. Resonance forms of deprotonated pyridones **1** and **2**.

gether with the correlation R^2 values (Supplementary material). The presented results confirm that this dipole-dipole interaction significantly increases the calculated torsion angle in compounds **1 · 2H$_2$O** and **2 · 4H$_2$O** to 53.65 and 56.76°, respectively. Also, the correlations of the experimental and calculated bond lengths demonstrate a significant influence of this interaction on the calculated bond lengths in the molecules, which improves the quality of the correlations on $R^2 = 0.9373$ for **1g** and $R^2 = 0.9570$ for **2g** and the SD is below 0.02.

According to the above-mentioned results, it is possible to assume that simulation of a larger number of these polar interactions would further increase the quality of the calculated data, but simulations with a larger number of explicitly added solvent molecules bonded with weak intermolecular interactions are computationally demanding and unpredictable. On the other side, the optimization of the molecular structure in a polar environment can be easily done using the self-consistent reaction field (SCRF) method which is commonly used for the modeling of the solvent effects [59]. In order to evaluate the effects of a different polar environment on the molecular structure of compounds **1b** and **2b**, the SCRF calculations based on the CPCM model [43,44] has been performed. The calculated bond lengths, C1–C2–N2–C6 torsion angle, dipole moments of compounds **1** and **2** in solvents of different polarity (ε) are given in Tables S4 and S5. By analysing the presented results, it can be seen that after the introduction of the CPCM model in the optimization, even for the simulation of non-polar n-hexane ($\varepsilon = 1.88$), the obtained results agree much better with the experimental values than for the isolated molecules in the vacuum. The quality of correlations between experimental and calculated bond lengths increases to $R^2 = 0.9242$ and 0.9462 which is at the same correlation level as for systems **1d** and **2d** with a larger number of explicit molecules bounded by intermolecular hydrogen bonds. Significant increases of the torsion angles (48.86 and 50.89°) as well as dipole moments (13.29 and 14.53 D) are also noticeable. An additional increase of solvent polarity $2 < \varepsilon < 25$ leads to a significant increase in the correlation qualities, while for $\varepsilon > 25$ the increase in the quality of correlation becomes less noticeable. The best correlation for the studied molecules was obtained with the simulation of water ($\varepsilon = 78.36$) as the solvent, $R^2 = 0.9628$ and 0.9764. The calculated torsion angles, 61.81 and 67.56°, agree well with the experimentally determined ones, and the dipole moments are significantly higher than for the compounds optimized in the vacuum (17.84 and 19.23 D). The analysis of the NBO charges for compound **1** (see Table S3) shows that in the zwitterionic form (**1b**) in vacuum, only 0.421 e is located on the pyridone scaffold *i.e.* that the displacement of the charge density towards the pyridinium scaffold is 0.579 e (torsion angle is 44.2°). The same compound in water as the solvent shows that 0.627 e is located on the pyridone scaffold *i.e.* that the displacement of the charge density towards the pyridinium scaffold is only 0.373 e. This decrease in delocalization (resonance) leads to greater polarization within the molecules and thus to a significant increase in planarity distortion.

Since the explicit and implicit simulations of interactions have shown a positive effect on the quality of the calculated geometric values for the studied compounds, it is logical to assume that combining these two approaches would also further contribute to their even more accurate determination. To verify this, systems **1e** and **2f**, with the maximum number of hydrogen bonds, are re-optimized with the CPCM model for the simulation of a polar environment (water). The obtained results presented in Tables S4 and S5 show excellent correlations of bonds lengths $R^2 = 0.9819$ and 0.9921 for compounds **1 · 2H$_2$O** and **2 · 4H$_2$O** as well as standard deviations under 0.01 Å for both systems. At the same time, the calculated torsion angles are significantly higher (68.08 and 81.74°) than in the crystal structures. Also, it should be pointed out that we encountered large problems with convergence during the optimization of system **2f**.

4. Conclusion

As state-of-the-art showed zwitterion hydrates receive much attention from the applicability point of view, while forming a variety of supramolecular networks. Herein, two pyridone based zwitterionic hydrates, **1 · 2H$_2$O** and **2 · 4H$_2$O**, and their crystal structures are revealed. Considering the pyridinium scaffold as an electron deficient scaffold was used as a building block, new motifs arise.

Two hydrates mainly differ in pyridinium moieties, wherein **1 · 2H$_2$O** is obtained with a pyridinium substituent, and **2 · 4H$_2$O** with 3,5-dimethylpyridinium one. The slight enlargement of the torsion angle of **2 · 4H$_2$O** compared to that of **1 · 2H$_2$O** is noticed and it is ascribed to two methyl groups introduced, whereas molecular geometry and bond lengths are not significantly affected. However, DFT computation showed that the torsion angle, in fact has an impact on molecular geometry and the network.

Both architectures are governed by dipole-dipole interactions, strong hydrogen bonds, weak ones with directing capability, π–π and C–H$\cdots\pi$ interactions. Dispersion plays an important role in the network governing **1 · 2H$_2$O** to form tubes and **2 · 4H$_2$O** into layers. Both structures have a recognizable $R_2^2(8)$ ring forged by inversion related dimers *via* N–H$\cdots$O hydrogen bonds. In the network of **1 · 2H$_2$O** two infinite chains of zwitterionic molecules form a tube, wherein the chain along the *c*-axis is dispersion driven, whereas the one along the *a*-axis is hydrogen bonded. The hollow spaces that are the result of the two chains interlacing in the 3D space are filled in tetrameric water structural segments forming water channels. On the other hand, zwitterions of **2 · 4H$_2$O** are dispersion driven along the *c*-axis into infinite chains interlacing with the ones along the *a*-axis formed by dimeric $R_2^2(8)$ rings and π–π interactions between pyridinium scaffolds. The interlacing of the chains leads to the formation of the zwitterionic layer. The methyl groups of **2 · 4H$_2$O** cause the steric hindrance resulting in the larger offset of the scaffolds. The edge-fused hexameric and tetrameric water pseudo rings of **2 · 4H$_2$O** forge water channels further connected into the water layer *via* interlayer contacts and one more water molecule (W4). In the overall contribution of individual interactions obtained by Hirshfeld analysis, O$\cdots$H contacts are found to have the main contribution in stabilizing the networks. On the other hand, the molecular network of **1 · 2H$_2$O** is more influenced by π–π interactions than the molecular network of **2 · 4H$_2$O** as a result of the larger offset of scaffolds caused by the methyl groups, whereas C–H$\cdots\pi$ contacts contribute more to the stabilization of the packing of **2 · 4H$_2$O**.

Computational analysis proved that the accuracy of molecular geometry is dependent on the number and strength of included intermolecular bonds, as well as on the number and position of molecules (zwitterions and water) included in the investigated systems. The simulation of compound solvation with the CPCM model also leads to better correlations. Furthermore, the combined approach of explicit and implicit simulations of interactions led to the much accurate determination of bond lengths and consequently to the best correlation results.

Declaration of Competing Interest

The authors declare that they have no known competing financial interests or personal relationships that could have appeared to influence the work reported in this paper.

CRediT authorship contribution statement

Aleksandra D. Mašulović: Investigation, Conceptualization, Visualization, Writing – original draft, Writing – review & editing. **Jelena M. Lađarević:** Investigation, Methodology, Validation. **Lidija D. Radovanović:** Investigation, Methodology, Validation. **Željko J. Vitnik:** Software, Conceptualization, Supervision, Writing – original draft. **Vesna D. Vitnik:** Software, Validation, Writing – original draft. **Jelena R. Rogan:** Investigation, Validation, Supervision. **Dušan Ž. Mijin:** Investigation, Validation, Supervision, Writing – original draft, Writing – review & editing.

Acknowledgments

This work was supported by the Ministry of Education, Science and Technological Development of the Republic of Serbia (Contract No. 451-03-9/2021-14/200287, 451-03-9/2021-14/200026 and 451-03-9/2021-14/200135).

Supplementary materials

Supplementary material associated with this article can be found, in the online version, at doi:10.1016/j.molstruc.2021.130419.

References

[1] S. Kohmoto, S. Okuyama, N. Yokota, M. Takahashi, K. Kishikawa, H. Masu, I. Azumaya, Generation of zwitterionic water channels: biszwitterionic imidazolium carboxylates as hydrogen-bonding acceptors, Cryst. Growth Des. 11 (2011) 3698–3702, doi:10.1021/cg200232b.
[2] J. van de Streek, J. Rantanen, A.D. Bond, Structures of cefradine dihydrate and cefaclor dihydrate from DFT-D calculations, Acta Cryst. C69 (2013) 1229–1233, doi:10.1107/S0108270113026863.
[3] S.P. Stokes, C.C. Seaton, K.S. Eccles, A.R. Maguire, S.E. Lawrence, Insight into the mechanism of formation of channel hydrates via templating, Cryst. Growth Des. 14 (2014) 1158–1166, doi:10.1021/cg401660h.
[4] K. Wzgarda-Raj, M. Palusiak, S. Wojtulewski, A.J. Rybarczyk-Pirek, The role of sulfur interactions in crystal architecture: experimental and quantum theoretical studies on hydrogen, halogen, and chalcogen bonds in trithiocyanuric acid–pyridine N-oxide co-crystals, CrystEngComm 23 (2021) 324–334, doi:10.1039/D0CE01319F.
[5] K.A. Lyssenko, Y.V. Nelyubina, R.G. Kostyanovsky, M.Y. Antipin, Water clusters in crystal: beyond the “hydrogen-bonding graphs”, Chem. Phys. Chem. 7 (2006) 2453–2455, doi:10.1002/cphc.200600549.
[6] D.E. Braun, M. Lampl, K. Wurst, V. Kahlenberg, U.J. Griesser, H. Schottenberger, Computational and analytical approaches for investigating hydrates: the neat and hydrated solid-state forms of 3-(3-methylimidazolium-1-yl)propanoate, CrystEngComm 20 (2018) 7826–7837, doi:10.1039/C8CE01565A.
[7] A.J. Savyasachi, O. Kotova, S. Shanmugaraju, S.J. Bradberry, G.M. Ó'Máille, T. Gunnlaugsson, Supramolecular chemistry: a toolkit for soft functional materials and organic particles, Chem. 3 (2017) 764–811, doi:10.1016/j.chempr.2017.10.006.
[8] A. Lazić, N. Trišović, L. Radovanović, J. Rogan, D. Poleti, Ž. Vitnik, V. Vitnik, G. Uščumlić, Towards understanding intermolecular interactions in hydantoin derivatives: the case of cycloalkane-5-spirohydantoins tethered with a halogenated benzyl moiety, CrystEngComm 19 (2017) 469–483, doi:10.1039/C6CE02210C.
[9] N. Trišović, J. Antanasijević, J. Rogan, D. Poleti, T. Tóth-Katona, M. Salamonczyk, A. Jákli, K. Fodor-Csorba, Investigation of supramolecular architectures of bent-shaped pyridine derivatives: from a three-ring crystalline compound towards five-ring mesogens, New J. Chem. 40 (2016) 6977–6985, doi:10.1039/C6NJ01515H.
[10] I. Khan, P. Panini, S. Ud-Din Khan, U.Ali Rana, H. Andleeb, D. Chopra, S. Hameed, J. Simpson, Exploiting the role of molecular electrostatic potential, deformation density, topology, and energetics in the characterization of S···N and Cl···N supramolecular motifs in crystalline triazolothiadiazoles, Cryst. Growth Des. 16 (2016) 1371–1386, doi:10.1021/acs.cgd.5b01499.
[11] C.B. Aakeroy, A.M. Beatty, M. Zou, Building organic assemblies with 2-pyridone and dicarboxylic acids: relating molecular conformation and synthon stability to crystal structure, Cryst. Eng. 1 (1998) 225–241, doi:10.1016/S0025-5408(98)00197-4.
[12] C.B. Aakeory, A.M. Beatty, M. Nieuwenhuyzen, M. Zou, Organic assemblies of 2-pyridones with dicarboxylic acids, Tetrahedron 56 (2000) 6693–6699, doi:10.1016/S0040-4020(00)00488-9.
[13] J.M. Rawson, R.E.P. Winpenny, The coordination chemistry of 2-pyridone and its derivatives, Coordin. Chem. Rev. 139 (1995) 313–374, doi:10.1016/0010-8545(94)01117-T.
[14] Q. Li, L. Mitscher, L. Shen, The 2-pyridone antibacterial agents: bacterial topoisomerase inhibitors, Med. Res. Rev. 20 (2000) 231–293, doi:10.1002/1098-1128(200007)20:4⟨231::AID-MED1⟩3.0.CO;2-N.
[15] Y. Fujita, H. Oguri, H. Oikawa, Biosynthetic studies on the antibiotics PF1140: a novel pathway for a 2-pyridone framework, Tetrahedron Lett. 46 (2005) 5885–5888, doi:10.1016/j.tetlet.2005.06.115.
[16] A. Fassihi, D. Abedi, L. Saghaie, R. Sabet, H. Fazeli, G. Bostaki, O. Deilami, H. Sadinpou, Synthesis, antimicrobial evaluation and QSAR study of some 3-hydroxypyridine-4-one and 3-hydroxypyran-4-one derivatives, Eur. J. Med. Chem. 44 (2009) 2145–2157, doi:10.1016/j.ejmech.2008.10.022.
[17] G. Semple, B. Andersson, V. Chhajlani, J. Georgsson, M. Johansson, Å. Rosenquist, L. Swanson, Synthesis and biological activity of kappa opioid receptor agonists. Part 2: preparation of 3-aryl-2-pyridone analogues generated by solution- and solid-phase parallel synthesis methods, Bioorg. Med. Chem. Lett. 13 (2003) 1141–1145, doi:10.1016/S0960-894X(03)00033-7.
[18] R. Parreira, O. Abrahão Jr., S. Galembeck, Conformational preferences of non-nucleoside HIV-1 reverse transcriptase inhibitors, Tetrahedron 57 (2001) 3243–3253, doi:10.1016/S0040-4020(01)00193-4.
[19] P. Dragovich, T. Prins, R. Zhou, E. Brown, F. Maldonado, S. Fuhrman, L. Zalman, T. Tuntland, C. Lee, A. Patick, D. Matthews, T. Hendrickson, M. Kosa, B. Liu, M. Batugo, J. Gleeson, S. Sakata, L. Chen, M. Guzman, J. Meador, R. Ferre, S. Worland, Structure-based design, synthesis, and biological evaluation of irreversible human rhinovirus 3C protease inhibitors. 6. Structure−activity studies of orally bioavailable, 2-pyridone-containing peptidomimetics, J. Med. Chem. 45 (2002) 1607–1623, doi:10.1021/jm010469k.
[20] L. Hasvold, W. Wang, S. Gwaltney, T. Rockway, L. Nelson, R. Mantei, S. Fakhoury, G. Sullivan, Q. Li, N. Lin, L. Wang, H. Zhang, J. Cohen, W. Gu, K. Marsh, J. Bauch, S. Rosenberg, H. Sham, Pyridone-containing farnesyltransferase inhibitors: synthesis and biological evaluation, Bioorg. Med. Chem. Lett. 13 (2003) 4001–4005, doi:10.1016/j.bmcl.2003.08.058.
[21] E.D. Thorsett, L.H. Latimer, Therapeutic approaches to Alzheimer's disease, Curr. Opin. Chem. Biol. 4 (2000) 377–382, doi:10.1016/S1367-5931(00)00102-2.
[22] L. Chen, X. Liu, B. Xu, C. Sun, P. Tao, Synthesis and luminescent properties and theoretical investigation on electronic structure of nitrile-based 2-pyridone molecules, Spectrochim. Acta A 79 (2011) 1926–1930, doi:10.1016/j.saa.2011.05.092.
[23] V. Gerhardt, M. Bolte, 3-Cyano-6-hydroxy-4-methyl-2-pyridone: two new pseudopolymorphs and two cocrystals with products of an in situ nucleophilic aromatic substitution, Acta Crystalogr. C71 (2015) 19–25, doi:10.1107/S2053229614025819.
[24] K.C. Shortsleeves, M.M. Turnbull, C.B. Seith, E.N. Tripodakis, F. Xiao, C.P. Landee, L.N. Dawe, D. Garrett, G.D. Delgado, B.M. Foxman, Crystallographic and magnetic studies of the 2-pyridone/copper halide system, Polyhedron 64 (2013) 110–121, doi:10.1016/j.poly.2013.03.066.
[25] M. Ueda, T. Mochida, H. Mori, Pyridone derivatives carrying radical moieties: hydrogen-bonded structures, magnetic properties, and metal coordination, Polyhedron 52 (2013) 755–760, doi:10.1016/j.poly.2012.07.056.
[26] B. Osmialowski, E. Kolehmainen, S. Ikonen, K. Ahonen, M. Löfman, NMR crystallography of 2-acylamino-6-[1H]-pyridones: solid-state NMR, GIPAW computational, and single crystal X-ray diffraction studies, J. Mol. Struct. 1006 (2011) 678–683, doi:10.1016/j.molstruc.2011.10.034.
[27] A. Muller, M. Losada, S. Leutwyler, Ab initio benchmark study of $(2\text{-pyridone})_2$, a strongly bound doubly hydrogen-bonded dimer, J. Phys. Chem. A 108 (2004) 157–165, doi:10.1021/jp0361024.
[28] N. El'chishcheva, V. Shklyaev, Zh. Vnutskikh, T. Odegova, S. Chekryshkin, S. Dubrovina, Synthesis and antimicrobial activity of new mono-and biquaternized dipyridylethanes and dipyridylethylenes, Pharm. Chem. J. 44 (2010) 251–253, doi:10.1007/s11094-010-0442-5.
[29] J. Zhang, J.M. Shreeve, Time for pairing: cocrystals as advanced energetic materials, CrystEngComm 182 (2016) 6124–6133, doi:10.1039/C6CE01239F.
[30] B. Lu, X. Fang, D. Yan, Thermal oxide layer enhances crystallinity and mechanical properties for plasma-sprayed hydroxyapatite biomedical coatings, ACS Appl. Mater. Interfaces 12 (2020) 33465–33472, doi:10.1021/acsami.0c05035.
[31] D. Yan, D.G. Evans, Molecular crystalline materials with tunable luminescent properties: from polymorphs to multi-component solids, Mater. Horiz. 1 (2014) 46–57, doi:10.1039/C3MH00023K.
[32] B. Zhou, Q. Zhao, L. Tanga, D. Yan, Tunable room temperature phosphorescence and energy transfer in ratiometric co-crystals, Chem. Commun. 56 (2020) 7698–7701, doi:10.1039/d0cc02730h.
[33] G.S. Nichol, V.K. Kumirov, R. Vardanyan, V.J. Hruby, Proton sharing and transfer in some zwitterionic compounds based on 4-oxo-4-((1-phenethylpiperidin-4-yl)(phenyl)amino)alcanoic acids, CrystEngComm 12 (2010) 3651–3657, doi:10.1039/B923698H.
[34] B. Wicher, K. Pyta, P. Przybylski, M. Gdaniec, Solvates of Zwitterionic rifampicin: recurring packing motifs via nonspecific interactions, Cryst. Growth Des. 18 (2018) 742–754, doi:10.1021/acs.cgd.7b01121.
[35] W. M. Schwarz, US Pat., 5413630, 1995.
[36] G.M. Sheldrick, SHELXT – integrated space-group and crystal-structure determination, Acta Cryst. A 71 (2015) 3–8, doi:10.1107/S2053273314026370.
[37] M.C. Burla, R. Caliandro, B. Carrozzini, G.L. Cascarano, C. Cuocci, C. Giacovazzo, M. Mallamo, A. Mazzone, G. Polidori, Crystal structure determination and refinement *via* SIR2014, J. Appl. Crystallogr. 48 (2015) 306–309, doi:10.1107/S1600576715001132.
[38] L.J. Farrugia, WinGX and ORTEP for windows: an update, J. Appl. Crystallogr. 45 (2012) 849–854, doi:10.1107/S0021889812029111.
[39] M.J. Frisch, G.W. Trucks, H.B. Schlegel, G.E. Scuseria, M.A. Robb, J.R. Cheese-

man, G. Scalmani, V. Barone, B. Mennucci, G.A. Petersson, H. Nakatsuji, M. Caricato, X. Li, H.P. Hratchian, A.F. Izmaylov, J. Bloino, G. Zheng, J.L. Sonnenberg, M. Hada, M. Ehara, K. Toyota, R. Fukuda, J. Hasegawa, M. Ishida, T. Nakajima, Y. Honda, O. Kitao, H. Nakai, T. Vreven, J.A. Montgomery, J.E. Peralta Jr., F. Ogliaro, M. Bearpark, J.J. Heyd, E. Brothers, K.N. Kudin, V.N. Staroverov, R. Kobayashi, J. Normand, K. Raghavachari, A. Rendell, J.C. Burant, S.S. Iyengar, J. Tomasi, M. Cossi, N. Rega, J.M. Millam, M. Klene, J.E. Knox, J.B. Cross, V. Bakken, C. Adamo, J. Jaramillo, R. Gomperts, R.E. Stratmann, O. Yazyev, A.J. Austin, R. Cammi, C. Pomelli, J.W. Ochterski, R.L. Martin, K. Morokuma, V.G. Zakrzewski, G.A. Voth, P. Salvador, J.J. Dannenberg, S. Dapprich, A.D. Daniels, Ö. Farkas, J.B. Foresman, J.V. Ortiz, J. Cioslowski, D.J. Fox, Gaussian 09 (Revision D.01), Gaussian, Inc., Wallingford, CT, 2009.

[40] A.D. Becke, Density-functional thermochemistry. III. The role of exact exchange, J. Chem. Phys. 98 (1993) 5648–5652, doi:10.1063/1.464913.

[41] C. Lee, W. Yang, R.G. Parr, Development of the Colle-Salvetti correlation-energy formula into a functional of the electron density, Phys. Rev. B 37 (1988) 785–789, doi:10.1103/PhysRevB.37.785.

[42] S. Grimme, J. Antony, S. Ehrlich, H. Krieg, A consistent and accurate ab initio parametrization of density functional dispersion correction (DFT-D) for the 94 elements H-Pu, J. Chem. Phys. 132 (2010) 154104 1-19, doi:10.1063/1.3382344.

[43] V. Barone, M. Cossi, Quantum calculation of molecular energies and energy gradients in solution by a conductor solvent model, J. Phys. Chem. A 102 (1998) 1995–2001, doi:10.1021/jp9716997.

[44] M. Cossi, N. Rega, G. Scalmani, V. Barone, Energies, structures, and electronic properties of molecules in solution with the C-PCM solvation model, J. Comp. Chem. 24 (2003) 669–681, doi:10.1002/jcc.10189.

[45] E.D. Glendening, A.E. Reed, J.E. Carpenter, F. Weinhold, NBO Version 3.1, TCI, University of Wisconsin, Madison, WI, 1998.

[46] A. Gavezzotti, Calculation of intermolecular interaction energies by direct numerical integration over electron densities. 2. An improved polarization model and the evaluation of dispersion and repulsion energies, J. Phys. Chem. B 107 (2003) 2344–2353, doi:10.1021/jp022288f.

[47] A. Gavezzotti, Non-conventional bonding between organic molecules. The 'halogen bond' in crystalline systems, Mol. Phys. 106 (2008) 1473–1485, doi:10.1080/00268970802060674.

[48] M.A. Spackman, D. Jayatilaka, Hirshfeld surface analysis, CrystEngComm 11 (2009) 19–32, doi:10.1039/B818330A.

[49] M.A. Spackman, J.J. McKinnon, Fingerprinting intermolecular interactions in molecular crystals, CrystEngComm 4 (2002) 378–392, doi:10.1039/B203191B.

[50] S.K. Wolff, D.J. Grimwood, J.J. McKinnon, M.J. Turner, D. Jayatilaka, M.A. Spackman, CrystalExplorer (Version 3.1), University of Western Australia, 2012.

[51] J. Mirković, B. Božić, V. Vitnik, Ž. Vitnik, J. Rogan, D. Poleti, G. Uščumlić, D. Mijin, Structural, spectroscopic and computational study of 5-(substituted phenylazo)-3-cyano-1-ethyl-6-hydroxy-4-methyl-2-pyridones, Color. Technol. 134 (2017) 33–43, doi:10.1111/cote.12321.

[52] F.H. Allen, O. Kennard, D.G. Watson, Tables of bond lengths determined by X-ray and neutron diffraction. Part 1. Bond lengths in organic compounds, J. Chem. Soc. Perkin. Trans. S1 (1987) 1–2, doi:10.1039/P298700000S1.

[53] C. Parkanyi, W.C. Herndon, Bond lengths and bond orders in π-electron heterocycles, Phosphorus Sulfur 4 (1978) 1–7, doi:10.1080/03086647808079955.

[54] P. Panini, T.P. Mohan, U. Gangwar, R. Sankollid, D. Chopra, Quantitative crystal structure analysis of 1,3,4-thiadiazole derivatives, CrystEngComm 15 (2013) 4549–4564, doi:10.1039/c3ce40278a.

[55] Z. Li, S. Chen, C. Gao, Z. Yang, K. Shih, Z. Kochovski, G. Yang, L. Gou, M. Nieh, M. Jiang, L. Zhang, G. Chen, Chemically controlled helical polymorphism in protein tubes by selective modulation of supramolecular interactions, J. Am. Chem. Soc. 141 (2019) 19448–19457, doi:10.1021/jacs.9b10505.

[56] P. Panini, K.N. Venugopala, B. Odhav, D. Chopra, Polymorphism in two biologically active dihydropyrimidinium hydrochloride derivatives: quantitative inputs towards the energetics associated with crystal packing, Acta Crystallogr. B 70 (2014) 681–696, doi:10.1107/s2052520614006209.

[57] M.P. Johansson, J. Olsen, Torsional barriers and equilibrium angle of biphenyl: reconciling theory with experiment, J. Chem. Theory Comput. 4 (2008) 1460–1471, doi:10.1021/ct800182e.

[58] O.V. Shishkin, I.S. Konovalova, R.I. Zubatyuk, G.V. Palamarchuk, S.V. Shishkina, A.V. Biitseva, I.V. Rudenko, V.A. Tkachuk, M.Yu. Kornilov, O.V. Hordiyenko, J. Leszczynski, Remarkably strong polarization of amidine fragment in the crystals of 1-imino-1H-isoindol-3-amine, Struct. Chem. 24 (2013) 1089–1097, doi:10.1007/s11224-012-0131-y.

[59] R.S. Corrêa, M.H. dos Santos, T.J. Nagem, J. Ellena, Host–guest interactions between xanthones and water: the role of O–H$\cdots$O, C–H$\cdots$O, and $\pi\cdots\pi$ contacts in the channel- and cage-type frameworks, Struct. Chem. 23 (2012) 1809–1818, doi:10.1007/s11224-012-9983-4.